

NATIONAL AERONAUTICS AND SPACE ADMINISTRATION

TECHNICAL REPORT
R-125

JET EFFECTS ON ANNULAR BASE PRESSURE AND TEMPERATURE IN A SUPERSONIC STREAM

By MILTON A. BEHEIM, JOHN L. KLANN,
and RICHARD A. YEAGER

COPY
FILE

1962

TECHNICAL REPORT R-125

JET EFFECTS ON ANNULAR BASE PRESSURE AND TEMPERATURE IN A SUPERSONIC STREAM

**By MILTON A. BEHEIM, JOHN L. KLANN,
and RICHARD A. YEAGER**

**Lewis Research Center
Cleveland, Ohio**

TECHNICAL REPORT R-125

JET EFFECTS ON ANNULAR BASE PRESSURE AND TEMPERATURE IN A SUPERSONIC STREAM

By MILTON A. BEHEIM, JOHN L. KLANN, and RICHARD A. YEAGER

SUMMARY

A theoretical and experimental investigation of jet-stream interaction effects on annular base pressure and temperature has been conducted. Eight single-jet nozzle configurations of varying design were studied: four of these used unheated air as the propellant fluid and were investigated at a free-stream Mach number of 2.0; the others employed a hydrogen peroxide rocket system and were investigated at Mach 2.0 and 1.6.

For ratios of jet total to base static pressure equal to or greater than design, predicted base-pressure ratios were generally less than the experimental values and were in closer agreement with results for the conical and shortened isentropic nozzles than with the results for full-length isentropic nozzles. In general the predicted base-temperature ratios were greater than the experimental values, and the deviation decreased with increasing jet-pressure ratio. This deviation was less at Mach 1.6 than at Mach 2.0 and was less with high-area-ratio nozzles than with low-area-ratio designs. The effect of base bleed on base-pressure ratio could be predicted with good accuracy in the range of bleed flows for which the bleed momentum could be neglected.

INTRODUCTION

The base flow resulting from the mutual interaction of exhaust jets and/or from the interaction of exhaust jets and the external stream is of interest to aircraft and missile designers because of its influence on base drag and heating. This general type of flow has proved to be difficult to treat analytically, but such an analysis would be of value in predicting base conditions for a specific design and in determining the significant flow

parameters that need to be considered in experimental studies. In recent years analytical techniques have progressed to the point where it is possible to predict base gas temperatures and pressures of simple configurations, and these techniques are explored in the present study of single-jet interaction with an external stream.

Up to this time most analyses of base pressure have employed the theoretical flow model described in references 1 and 2 for uniform total temperature. Theoretical results have shown good correlation with data for two-dimensional flows with turbulent mixing (e.g., refs. 2 to 4). Jet effects on annular base pressures in a supersonic stream were determined experimentally in the study of reference 5 with small-scale models, and results were compared with theoretical predictions obtained from a modified version of this flow model. The correlation is good for convergent nozzles but not for convergent-divergent nozzles. The present study extends this work of reference 5 with convergent-divergent nozzles and differs chiefly in that larger scale models were used for the experimental data and effects of base bleed were included.

The adaptation to the flow model that is required to account for nonuniform total-temperature effects to permit a calculation of base gas temperature is described in references 6 and 7. The limited base-pressure and -temperature data presented in reference 6 for a two-dimensional rearward facing step show good correlation with theory. In the present study the axisymmetric flow model of reference 5 has been adapted to account for jet total-temperature effects, and results are compared with experimental base-gas

temperatures and pressures of hydrogen peroxide rocket motors in a supersonic stream.

FLOW MODEL

The essential details of the flow model used in the base-flow analysis of this report are shown in figure 1. Figures 1 (a) and (b) illustrate the flow patterns with underexpanded ($p_j > p_b$) and overexpanded ($p_j < p_b$) jets, respectively. In either case the jet and the stream total pressures, total temperatures, and gas properties (γ and R) may be at arbitrary and differing values. (Symbols are defined in appendix A.) It is assumed that the nozzle is flowing full for both the overexpanded and the underexpanded jet, and that in either case the external and internal streams expand or compress to base pressure immediately downstream of the base surface. Neglecting for the moment the effects of mixing, the shapes of the boundaries

(referred to as the free streamlines) of the two axisymmetric streams downstream of the base may be determined by methods in the literature (or in the case of the overexpanded jet, by modifications of these methods). At the point of intersection of the external and internal streams there are trailing shock waves which deflect the two streams so that the static pressures and flow directions downstream of the intersection are equal for both streams. It is assumed that the pressure rise of the trailing shock waves corresponds to that of a simple plane wave that deflects the flow direction of each stream from that of the free streamline just ahead of the intersection to the common value downstream of the intersection. As discussed in reference 4, these assumptions are an oversimplification of what actually occurs in axisymmetric flows, but they lead to important simplifications for numerical solutions of the base flow.

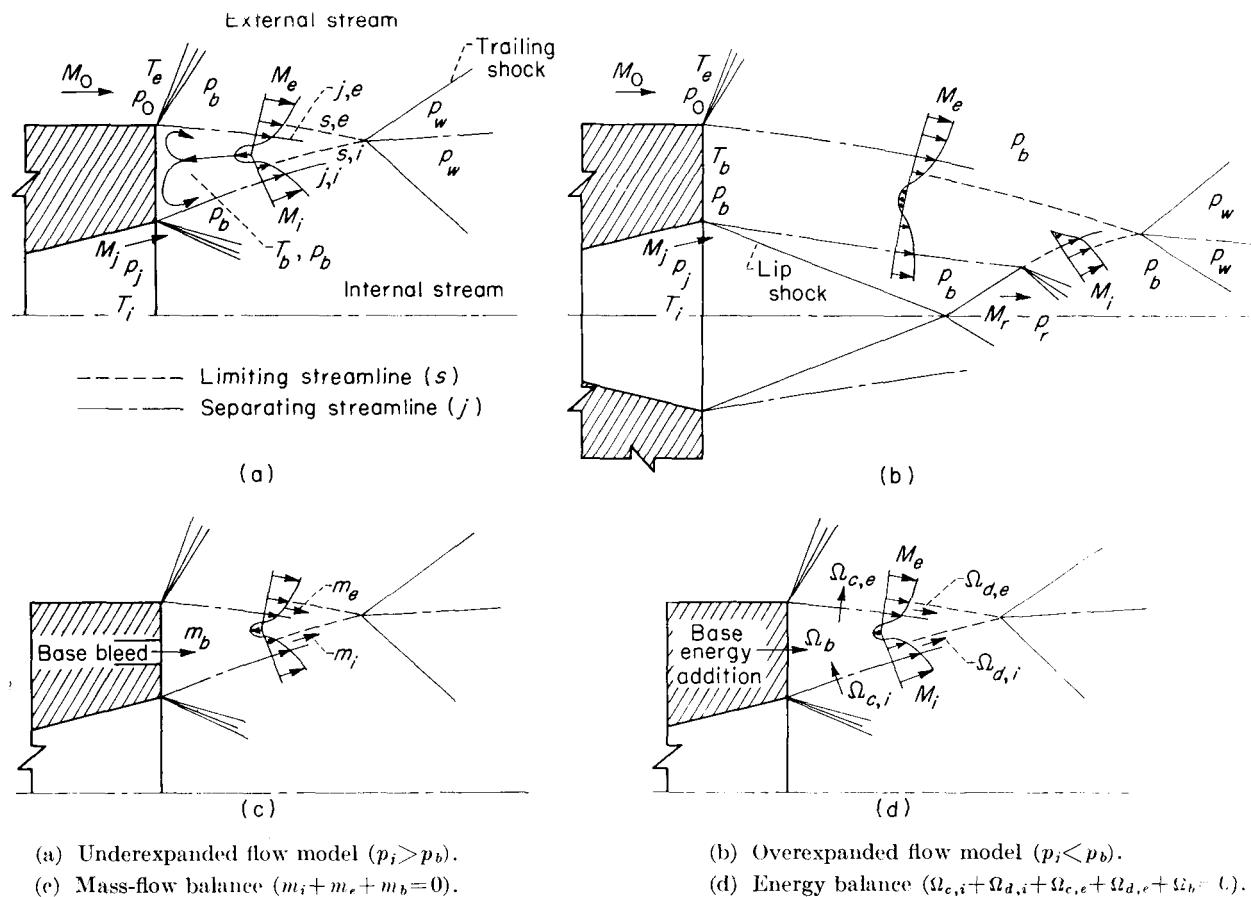


FIGURE 1.—Details of flow in base region.

The effects of mixing along the boundaries of the two streams are considered next. The usual assumptions are made that the mixing is turbulent and (in the nomenclature of ref. 6) is fully developed ahead of the trailing shock. Located within both the internal and external mixing profiles are two streamlines of special significance referred to as the limiting and the separating streamlines (and indicated in fig. 1). The separating streamline of the external flow is defined as that for which the integrated total flow rate external to it is equal to the total flow rate of the external stream upstream of the base. Similarly the separating streamline of the internal flow is that for which the integrated flow rate inside it is equal to the flow rate of the nozzle. A two-dimensional mixing profile of the type described in reference 6 (but modified to account for variations in gas properties through the profile as discussed in appendix B) is assumed to be superimposed upon the two streams so that the separating streamlines coincide with the free streamlines discussed earlier and so that the flow directions throughout the profiles are uniformly equal to the local values of the free streamlines. The limiting streamline of either stream is defined as that which when stagnated isentropically produces a static-pressure rise equal to that of the trailing shock wave. This pressure rise is equal for both the internal and external limiting streamlines. Thus all the flow outside the external limiting streamline and inside the internal limiting streamline has sufficient velocity to negotiate the pressure rise of the trailing shock waves and proceed downstream. However, the flow between the external and the internal limiting streamlines lacks sufficient total pressure to negotiate the pressure rise and hence reverses direction and flows back upstream toward the base surface. In calculating base pressure and gas temperature, it is necessary to determine locations of the internal and external limiting streamlines such that a mass-flow balance and an energy balance are satisfied for the base region. These balances are illustrated in figures 1(c) and (d), respectively, and, as discussed in appendix B, are obtained by means of a double trial-and-error solution assuming various values for the base pressure and temperature. Effects of base bleed and of base energy addition (such as by means of base burning or base heat transfer) may be included in the mass-flow and energy balances.

This analysis of appendix B was also applied in appendix C to determine analytically the effects of various independent geometric, aerodynamic, and thermodynamic variables on the wake-flow parameters, wake-pressure ratio, and base-temperature ratio. These variables were varied systematically to show trends of effects and to show conditions for which each variable had an important effect on base flow.

APPARATUS AND PROCEDURE

The experimental portion of this investigation was conducted in the Lewis 8- by 6-foot wind tunnel. Eight single-jet exhaust-nozzle configurations of varying design were studied in the supersonic test section of the tunnel. Four of these nozzles used unheated air as the propellant fluid and were investigated at a free-stream Mach number of 2.0; the other nozzles employed hydrogen peroxide and were investigated at free-stream Mach numbers of 2.0 and 1.6.

The wind-tunnel installation is sketched in figure 2. The model employed a 20° conical nose

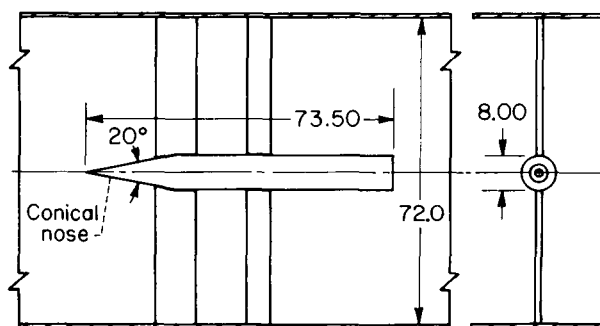


FIGURE 2.—Tunnel installation (dimensions in inches).

and two support struts normal to the body axis which spanned the 6-foot dimension of the test section.

COLD-JET MODELS

Unheated dried air was ducted through the support struts and straightened by means of a honeycomb before entering the nozzle. Four interchangeable nozzle configurations are shown in figure 3, three isentropic contoured nozzles with design pressure ratios P_j/p_e of 20, 50, and 100, and one 13.4° conical nozzle designed for a pressure ratio of 50. Henceforth these nozzles will be referred to by the design pressure ratio and the

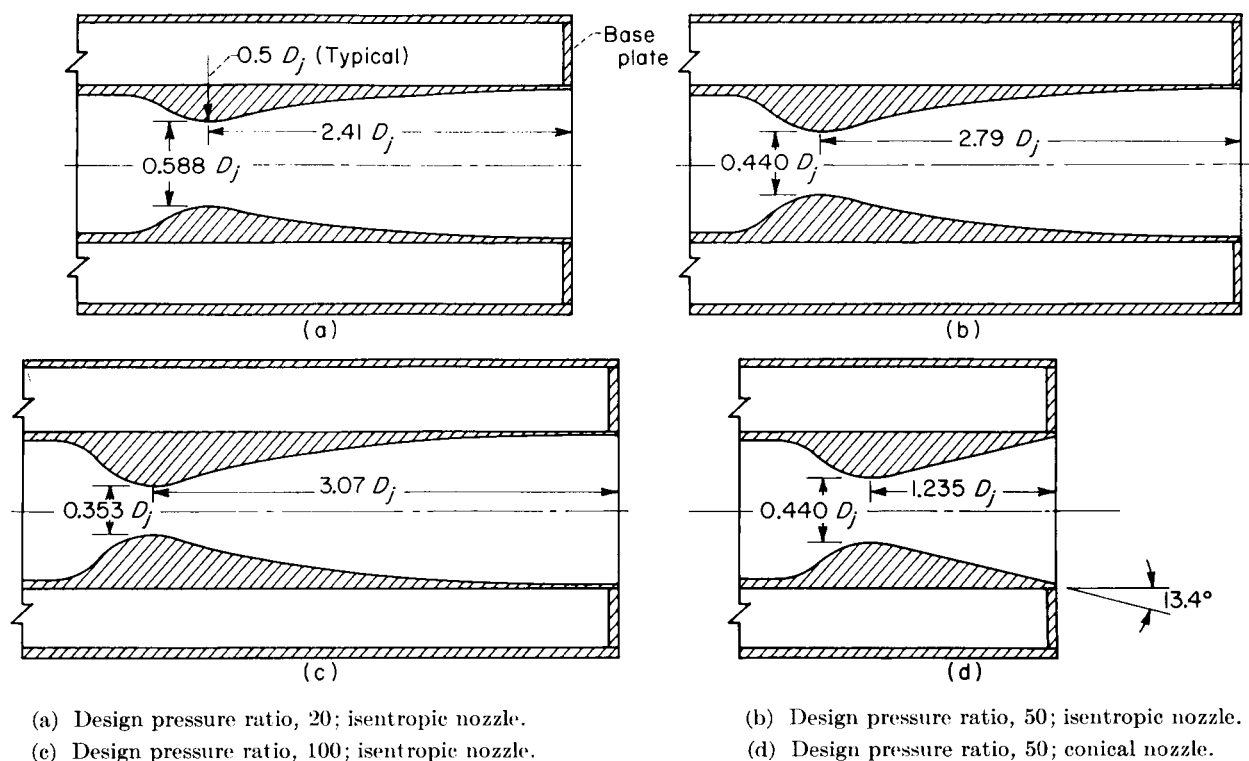


FIGURE 3.—Cold-jet nozzle configurations. Jet diameter D_j , 4 inches; base diameter ratio D_b/D_j , 2.0.

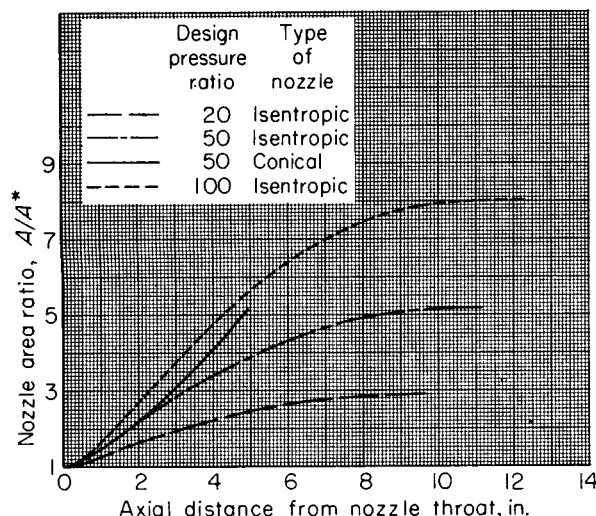


FIGURE 4.—Cold-jet nozzle area variations.

type of nozzle shape. The isentropic contours were determined by the approximate method of reference 8, and the resulting area variations for these and the conical nozzle are presented in figure 4. All four nozzles had 4-inch exit diam-

eters; hence all configurations had base- to jet-diameter ratios of 2.

To determine base-bleed effects the base plate was removed to permit passage of air through the annular opening between the nozzle and afterbody. A separate ducting arrangement through the struts was used to supply the bleed air from a source external to the tunnel.

The jet total pressure was determined with a 16-tube rake located downstream of the honeycomb, and jet exit static pressure from two orifices located about $\frac{1}{4}$ inch upstream of the exit plane. For the configurations with no base bleed, average base pressure was determined from eight orifices on the base plate located in the plane normal to that of the struts. With the open-base configurations for bleed studies, the eight base-pressure orifices were located on the inner surface of the afterbody about 1 inch upstream of the exit plane. Three Pitot tubes located in the bleed passage 3 inches upstream of the exit plane were used to measure bleed total pressure. Bleed-flow rates were determined with a standard ASME orifice.

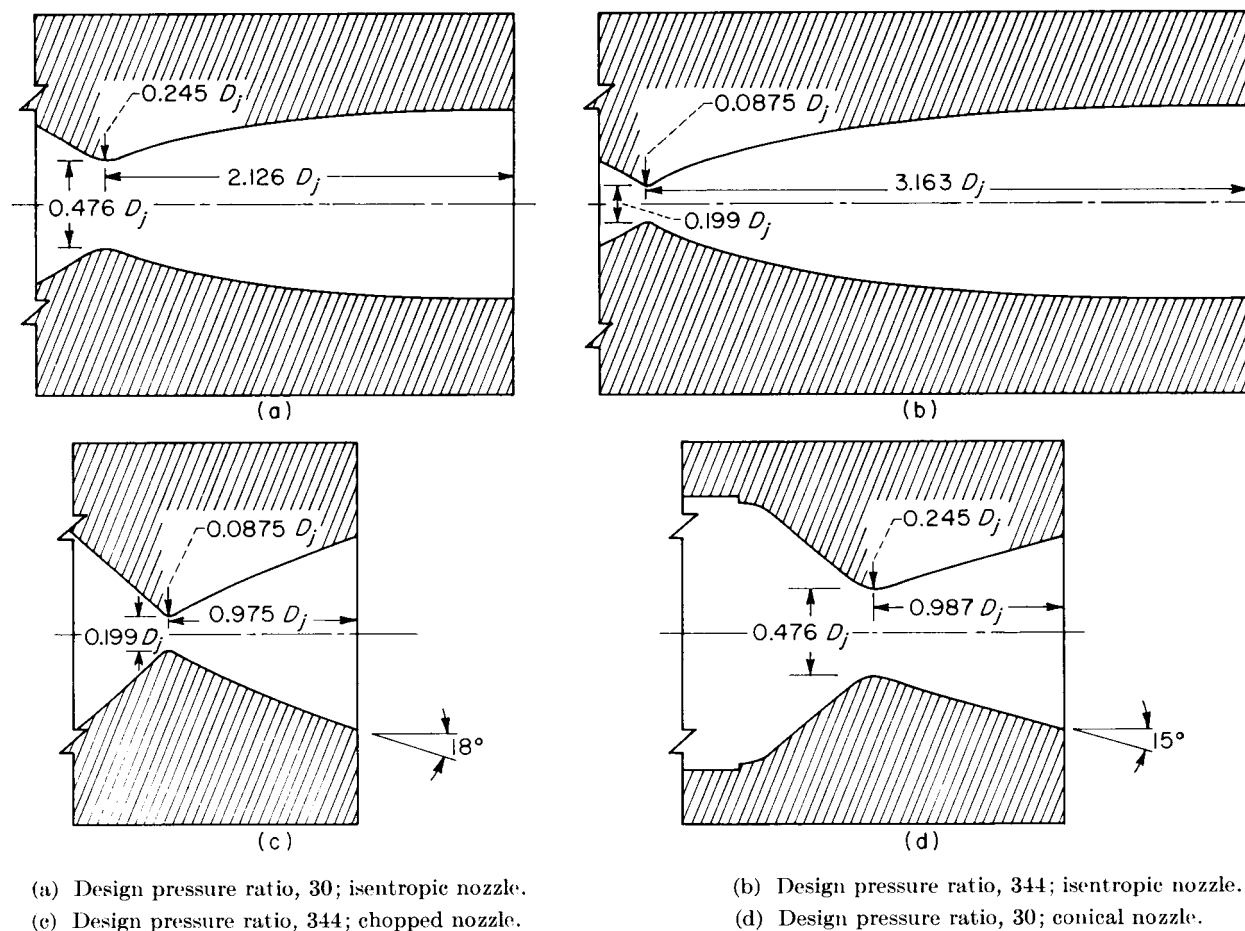


FIGURE 5.—Hot-jet nozzle configurations. Jet diameter D_j , 4 inches; base diameter ratio D_b/D_j , 2.0.

For a portion of the test, a survey of the base flow was conducted with translating Pitot rakes. One rake was mounted on the base plate, and a second rake was mounted from a strut downstream of the model.

HOT-JET MODELS

The hydrogen peroxide rocket system used was of the type described in detail in reference 9. The pressurized hydrogen peroxide entered a catalytic decomposition chamber of silver mesh screens which caused the decomposition of the peroxide into oxygen and steam. The 90 percent hydrogen peroxide and water mixture that was used resulted in the following jet characteristics: Total temperature T_j , 1820° R; ratio of specific heats γ_j , 1.27; specific gas constant R_j , 2249 ft²/(sec²)(°R). The cylindrical afterbody was

employed, and for all nozzles the base- to jet-diameter ratio was 2.

The details of the nozzles investigated are shown in figure 5. The wall contours of the isentropic nozzles were approximated by using the coordinates presented in reference 10 for $\gamma=1.4$ without correction for the change in γ . The resulting one-dimensional area ratios were such that, for $\gamma=1.27$, the design pressure ratios P_j/p_e were 30 (fig. 5(a)) and 344 (fig. 5(b)). To simulate a contoured nozzle with a more practical length than the full-length isentropic nozzles, the chopped nozzle design illustrated in figure 5(c) was employed. The isentropic contour presented in reference 10 for a nozzle with an area ratio of 217 was cut back so that the resulting one-dimensional exit area ratio and hence the design pressure ratio was the same as that of the 344

isentropic nozzle of figure 5(b). A pressure-ratio-30 conical nozzle (fig. 5(d)) was also employed. The area variations of the four nozzles are shown in figure 6.

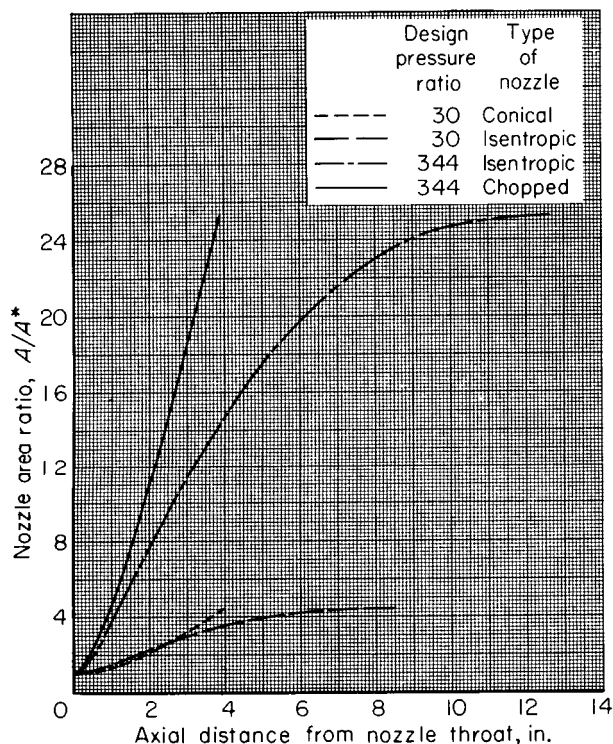


FIGURE 6.—Hot-jet nozzle area variations.

For all nozzles the external surface of the decomposition chamber and nozzle was wrapped with a water-cooling coil to protect instrumentation.

The jet total pressure and temperature were measured by three pressure transducers and three thermocouples located in the decomposition chamber. Static-pressure taps were located along the walls of the nozzles to determine internal pressure distributions, and the jet exit pressure was determined by three orifices located just upstream of the nozzle exit. Base-region instrumentation was located in the plane normal to that of the struts. The average base static pressure was measured with eight orifices on the base plate, and the average base temperature was obtained from eight thermocouples located $\frac{1}{4}$ inch from the base plate surface. For a portion of the test, temperature profiles downstream of the base were obtained with a translating thermocouple

rake which was strut-mounted downstream of the model. The hydrogen peroxide weight flow was determined with electronic flow meters.

RESULTS AND DISCUSSION

BASE-FLOW SURVEYS

Typical results from the base-flow surveys are presented in figures 7 and 8, and for comparison the free streamlines and trailing shock waves of the theoretical flow model have been superimposed upon the experimental data. Shown in figure 7 are velocity-ratio profiles for the cold-jet pressure-ratio-50 conical nozzle operating at a jet pressure ratio P_j/p_b of 62.3. For the calculation of local-to ideal-velocity ratio a local Mach number was computed using the ratio of local Pitot pressure to an assumed value of local static pressure. Upstream of the trailing shocks the local static pressure was assumed to be equal to the experimental base pressure, and downstream of the trailing shocks it was assumed equal to that of the theoretical flow model. The ideal velocity in each region was determined using the theoretical Mach number of the flow model at the edge of the mixing region. The origin (or base line) of the individual profiles shown in the figure indicates the location of the rake. Although the rakes were aligned axially with the model, the flow profiles are drawn parallel to the directions of the theoretical local free streamlines to clarify the presentation.

The free streamlines and trailing shock waves shown in figure 7 were determined by the procedures described in steps (1) and (2) of appendix B and using the experimental value of base-pressure ratio. External streamline coordinates were obtained from the characteristic solutions of reference 11, and the circular-arc approximation method of reference 12 was used to obtain internal streamline coordinates. The results show qualitative agreement between the theoretical flow model and the location of experimental velocity gradients.

Figure 8 presents typical total-temperature profiles downstream of the base of the 344 isentropic nozzle operating at a jet-pressure ratio of 350. In a manner similar to that of figure 7, the theoretical free streamlines and trailing shock waves of the flow model are also shown. For figure 8 the internal streamline coordinates were

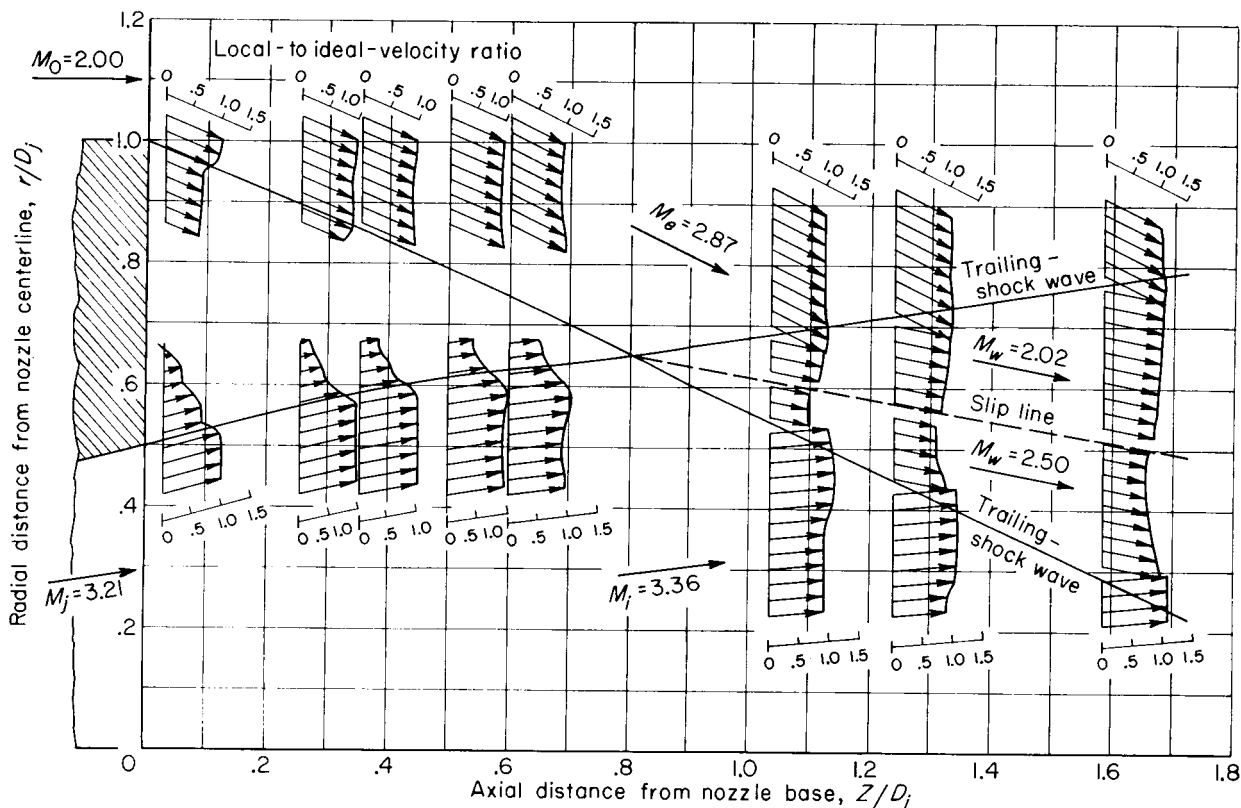


FIGURE 7.—Experimental cold-jet velocity distributions. Pressure-ratio-50 conical nozzle; jet-pressure ratio P_j/p_b , 62.3; base-pressure ratio p_b/p_0 , 0.260.

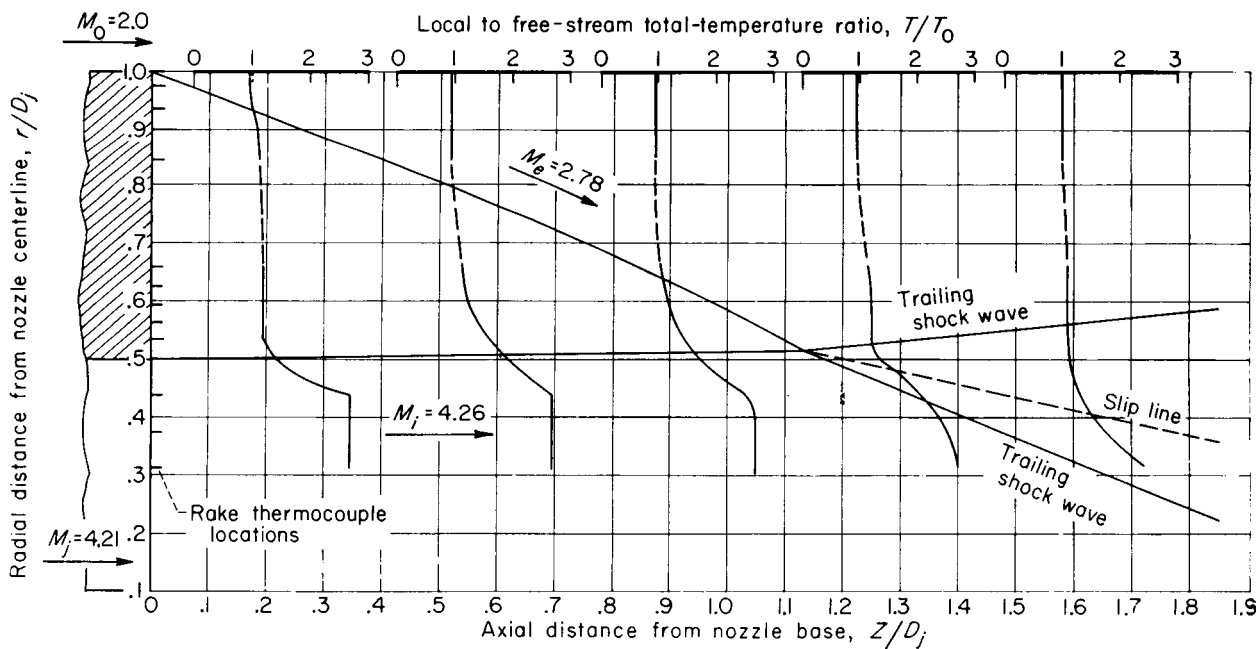
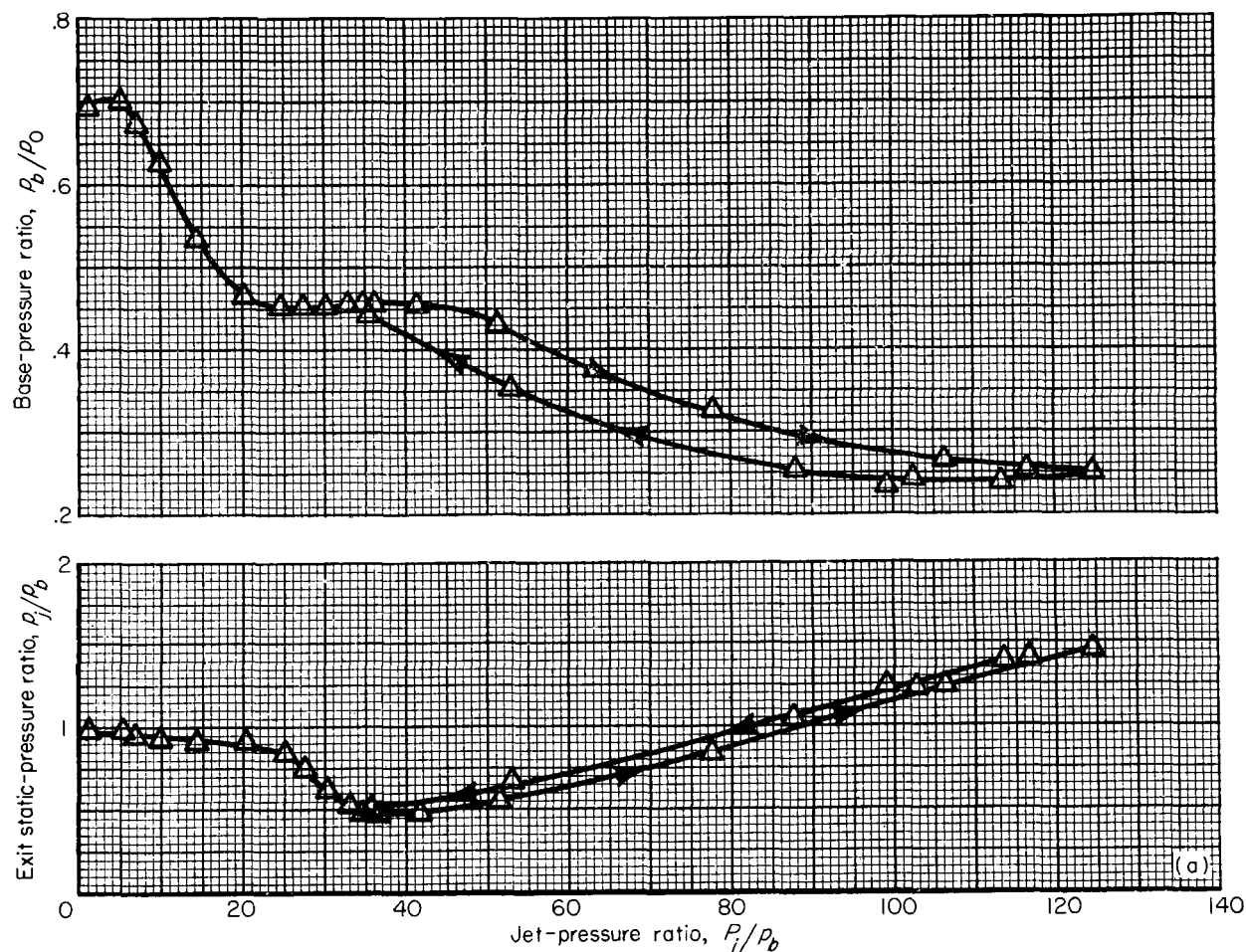


FIGURE 8.—Experimental hot-jet temperature distributions. Pressure-ratio-344 isentropic nozzle; jet-pressure ratio P_j/p_b , 350; base-pressure ratio p_b/p_0 , 0.289.



(a) Experimental base-pressure characteristics.

FIGURE 9.—Base-flow parameters of pressure-ratio-100 isentropic nozzle.

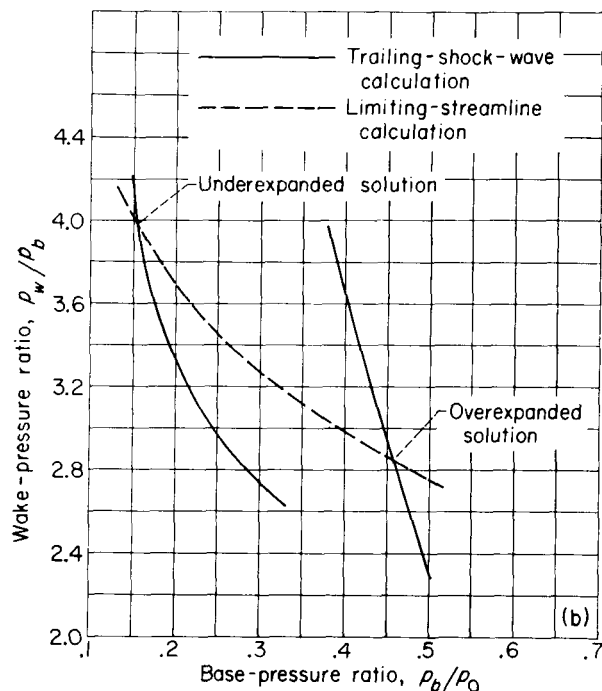
obtained from the characteristic solutions of reference 12. The trailing-shock-wave locations were determined by use of shock charts for the different specific-heat ratios of the internal and external streams. Figure 8 also shows good correlation between the location of experimental temperature gradients and the theoretical locations of the free streamlines and the slip line. Similar results were obtained over a range of jet-pressure ratio with all the nozzles investigated.

COLD-JET BASE PRESSURES

Experimental and theoretical base-region pressures of the cold-jet models at a free-stream Mach number of 2 are presented in figures 9 to 12. In figure 9(a) the experimental exit static-pressure ratio p_j/p_b and base-pressure ratio p_b/p_0 are

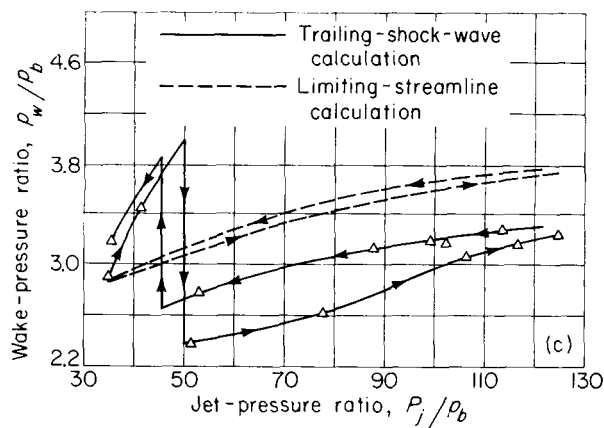
presented as functions of the jet-pressure ratio for the 100 isentropic nozzle. These results show that the nozzle flow was separated for jet-pressure ratios up to about 35 (decreasing p_j/p_b), that the nozzle was flowing full but was overexpanded in the pressure-ratio range from 35 to about 85 ($p_j/p_b < 1$ and increasing linearly with P_j/p_b), and that the nozzle flow was underexpanded for pressure ratios greater than 85 ($p_j/p_b > 1$). It is also apparent that a hysteresis loop existed in the base-flow characteristics; that is, the value of base-pressure ratio for a given value of jet-pressure ratio depended upon the direction in which the nozzle pressure had been varied.

Presented in figure 9(b) is a typical theoretical base-pressure solution for a given value of overall nozzle pressure ratio (for this example, $P_j/p_0 = 16$).



(b) Example solution for base-pressure ratio. Jet-pressure ratio P_j/p_0 , 16.0.

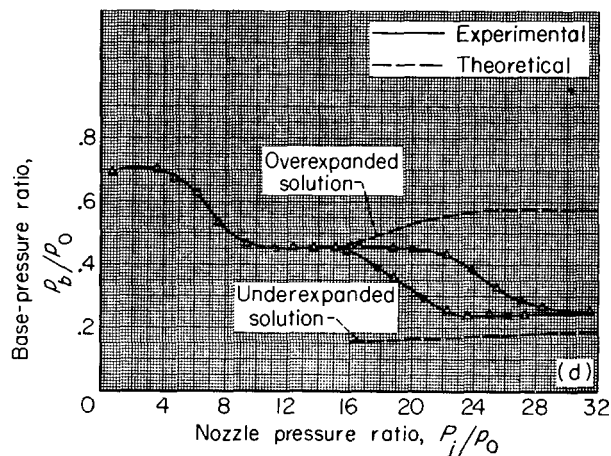
FIGURE 9.—Continued. Base-flow parameters of pressure-ratio-100 isentropic nozzle.



(c) Comparison of trailing-shock-wave and limiting-streamline wake-pressure ratios.

FIGURE 9.—Continued. Base-flow parameters of pressure-ratio-100 isentropic nozzle.

As described in appendix B, several values of base-pressure ratio are assumed, and the corresponding values of trailing-shock-wave and limiting-streamline wake-pressure ratios were determined. For the limiting-streamline calculation it was assumed that the jet and free-stream total



(d) Comparison of theoretical and experimental base-pressure ratios.

FIGURE 9.—Concluded. Base-flow parameters of pressure-ratio-100 isentropic nozzle.

temperatures were equal and that the mixing-length ratio X (defined as $\frac{x_i}{\sigma_i} \frac{x_e}{\sigma_e}$) was 1. (Values of X less than 1 generally are associated with configurations for which the rocket motor extends downstream of the base, and values of X greater than 1 correspond to geometries for which the outer shroud extends downstream of the jet exit.) Hence the charts of reference 5 were used. The base-pressure ratio for which the shock and streamline wake-pressure ratios are equal is then the theoretical value of base-pressure ratio.

As shown in figure 9(b), two solutions are possible for a given value of nozzle pressure ratio: one corresponding to the underexpanded flow pattern illustrated in figure 1(a) (at $p_b/p_0=0.16$), and another corresponding to the overexpanded flow pattern of figure 1(b) (at $p_b/p_0=0.46$). It is not known beforehand which solution will exist experimentally.

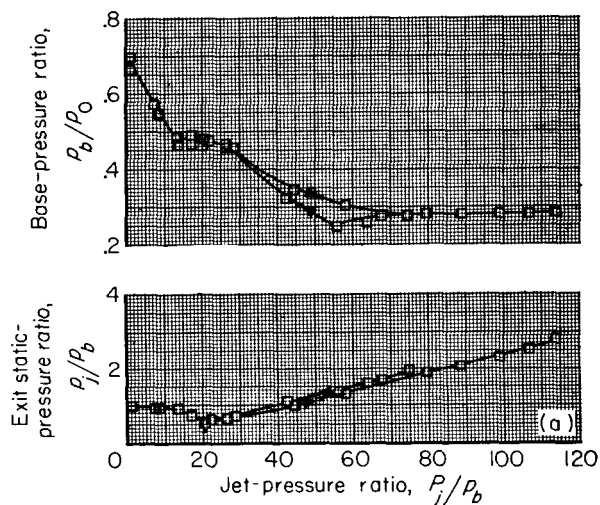
The theoretical ratios of trailing-shock-wave and limiting-streamline wake pressure corresponding to the experimental values of base-pressure ratio in figure 9(a) were computed by the procedures of appendix B. These calculations were made at jet-pressure ratios for which the nozzle was flowing full, and the results are shown in figure 9(c) for each branch of the hysteresis loop. As discussed in appendix B, the trailing-shock pressure rise depends upon the Mach numbers and flow directions of the internal and external free streamlines at their point of intersection,

whereas the limiting-streamline pressure rise depends only upon the Mach numbers. If the theoretical flow model exactly describes the experimental flow phenomena, the trailing-shock and the limiting-streamline wake-pressure ratios would be equal for a given jet-pressure ratio, as illustrated in figure 9(b). It is apparent that, in spite of the large number of assumptions that must be made in the flow model, the results were in fairly good agreement. For these calculations the external free streamline was again obtained from reference 11, and the internal free streamline was computed by the method of reference 13. The trailing-shock-wave solution shows a sharp increase in wake-pressure ratio for effective jet-pressure ratios less than about 50. This increase occurred because the origin of the trailing-shock waves had moved far enough downstream that the lip shock from the opposite side of the nozzle had produced a sharp change in flow direction of the internal free streamline upstream of the intersection of the internal and external streamlines. This situation is illustrated in figure 1(b). In the calculation this effect of the lip shock was approximated by assuming it to be a plane wave. The streamline shape downstream of the intersection was again obtained by the calculation procedure of reference 13 and with the assumption that the flow issued from a fictitious nozzle with an exit Mach number M_r (see fig. 1(b) for definition) and expanded through the pressure ratio p_r/p_b . As shown in figure 9(c), the lip shock effect was large on the trailing-shock solution, since the change in flow direction was large; but because the change in internal free-stream Mach number at the point of intersection of the external and the internal streamlines was small, the change in the limiting-streamline solution was negligible.

The procedure illustrated in figure 9(b) was repeated for a range of nozzle pressure ratio, and the resulting theoretical base-pressure ratios are compared with the experimental values in figure 9(d). At the lowest nozzle pressure ratios for which the nozzle was flowing full ($P_j/p_0=16$), the experimental base-pressure ratio was equal to the theoretical overexpanded solution. As nozzle pressure ratio increased, the experimental curves crossed over the region between the overexpanded and the underexpanded solutions, and at nozzle pressure ratios greater than design approached very closely the underexpanded solutions. In this

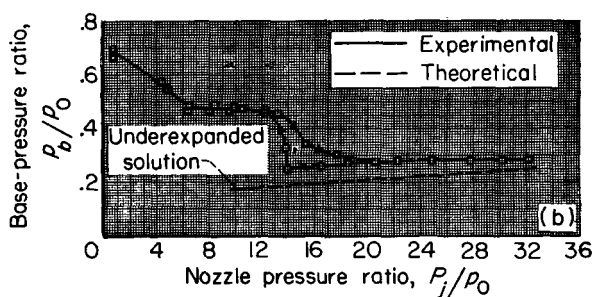
pressure-ratio range where the crossover occurred the hysteresis loop also occurred, and it is not clear what flow phenomena existed in order to yield experimental base pressures between the two solutions.

Data for the other cold-jet nozzles are presented in figures 10 to 12. Shown are the experimental



(a) Experimental base-pressure characteristics.

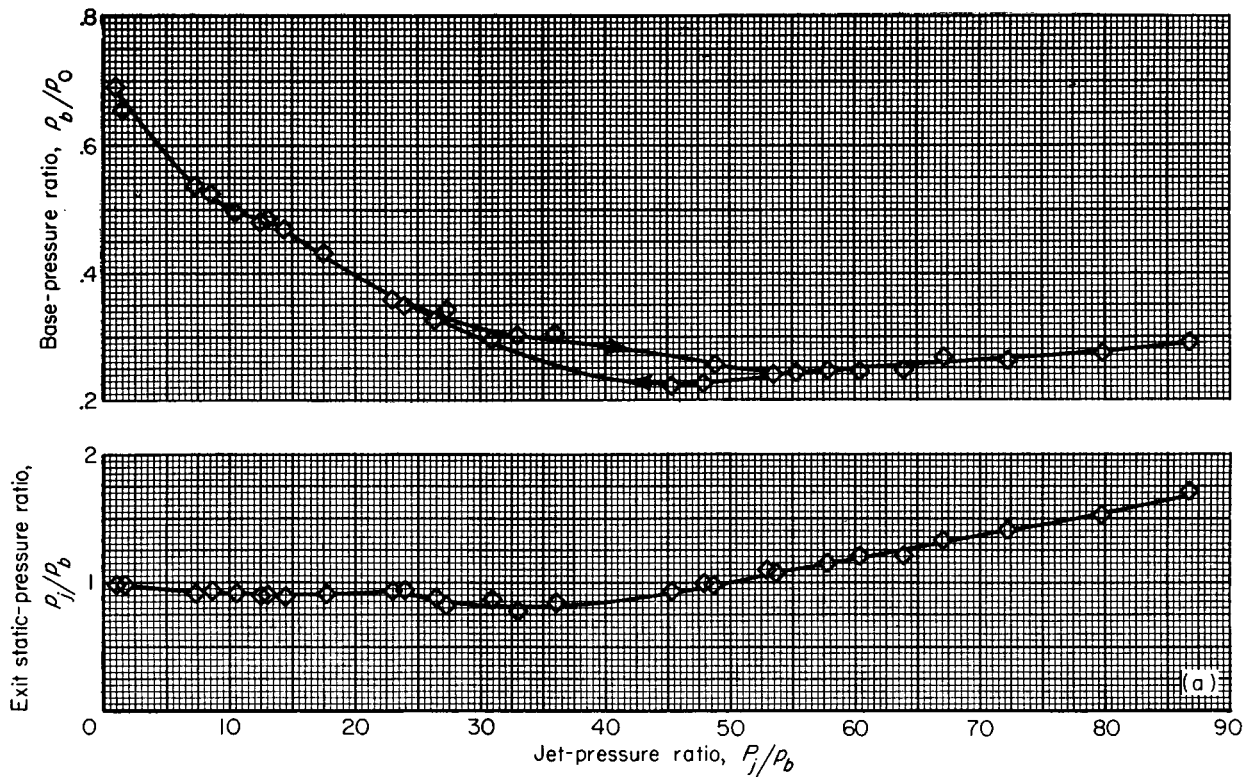
FIGURE 10.—Base-flow parameters of pressure-ratio-50 isentropic nozzle.



(b) Comparison of theoretical and experimental base-pressure ratios.

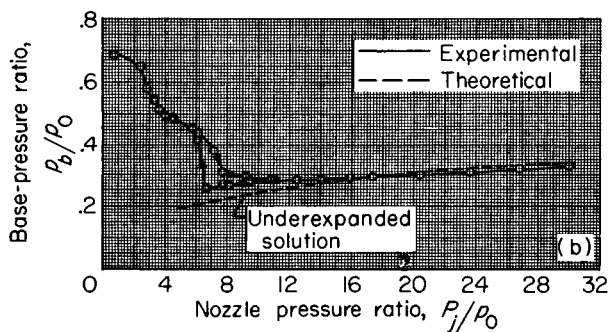
FIGURE 10.—Concluded. Base-flow parameters of pressure-ratio-50 isentropic nozzle.

base-pressure characteristics and the comparison of the theoretical underexpanded solutions with the experimental base-pressure ratios for the range of jet-pressure ratios for which there was not a lip shock and a free streamline interference effect. Because figure 9(d) had shown that the theoretical overexpanded solution is of significance only at low jet-pressure ratios, where the nozzle is flowing full, these solutions were not obtained for the



(a) Experimental base-pressure characteristics.

FIGURE 11.—Base-flow parameters of pressure-ratio-20 isentropic nozzle.



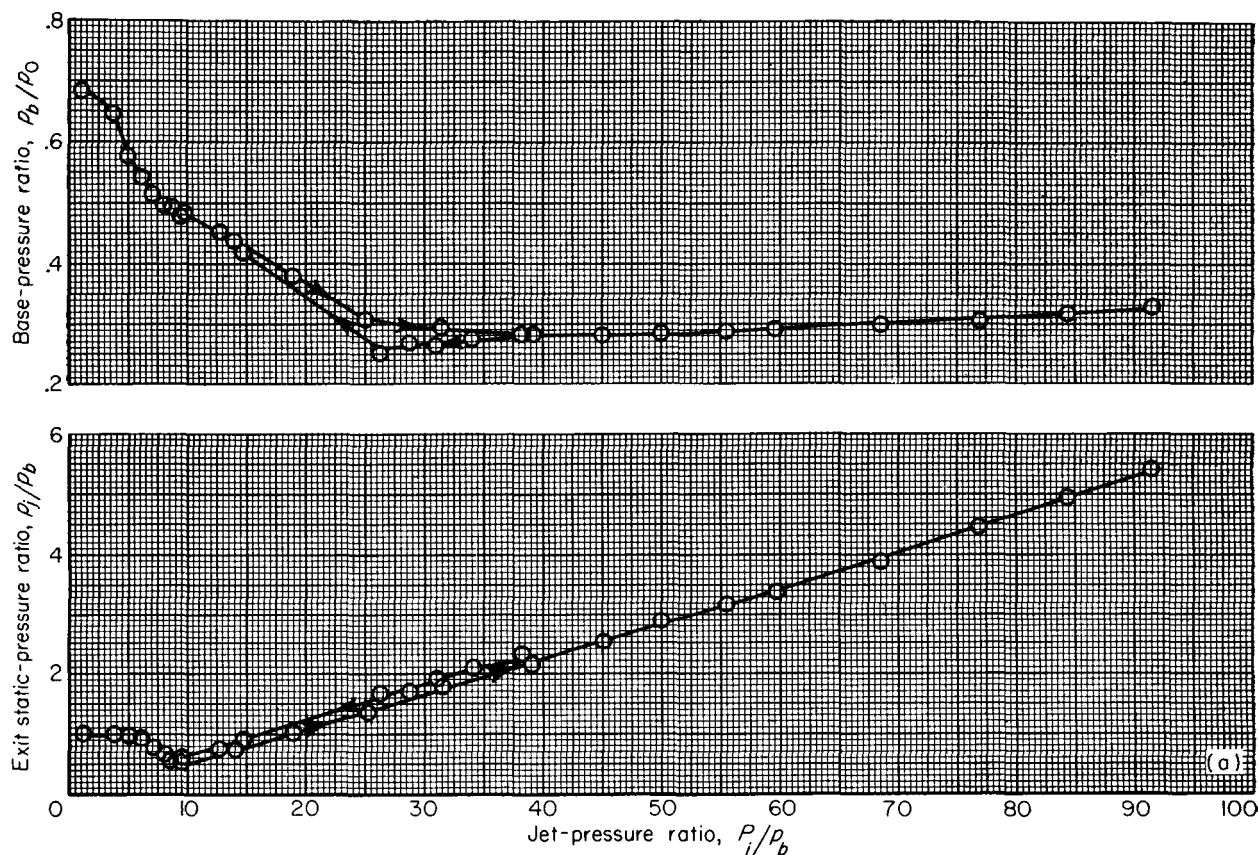
(b) Comparison of theoretical and experimental base-pressure ratios.

FIGURE 11.—Concluded. Base-flow parameters of pressure-ratio-20 isentropic nozzle.

nozzles of figures 10 to 12. Results were essentially the same as those discussed in figure 9: a hysteresis loop occurred at the lower jet-pressure ratios for which the nozzle was flowing full, and the experimental base-pressure ratios were close to the theoretical underexpanded solutions at jet-pressure ratios greater than design. In addition, for the isentropic nozzles the data for the low-

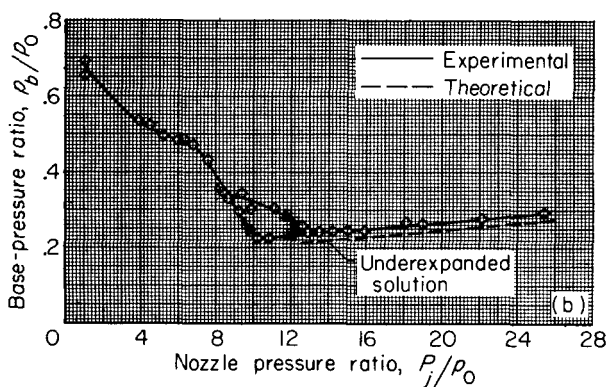
design-pressure-ratio nozzle (fig. 11(b)) agreed more closely with theory than did data for the high-pressure-ratio designs (figs. 9(d) and 10(b)). For the same design pressure ratio the conical-nozzle data (fig. 12(b)) showed better correlation with theory than those for the isentropic nozzle (fig. 10(b)). In all cases the external free streamline was determined from reference 11. For jet-pressure ratios less than design the internal free streamline was obtained from reference 13, and for jet-pressure ratios greater than design the circular-arc approximation of reference 12 was used.

It was determined that a parameter which correlated fairly well the difference between theory and experiment for all the nozzles was the ratio of jet to design pressure ratio $(P_j/p_0)/(P_j/p_0)_{des}$. Results are shown in figure 13 for the deviation between limiting-streamline and trailing-shock wake-pressure ratio. Data such as those presented in figure 9(c) were used in computing this deviation. The correlation was fairly good regardless of nozzle design and perhaps could be



(a) Experimental base-pressure characteristics.

FIGURE 12.—Base-flow parameters of pressure-ratio-50 conical nozzle.



(b) Comparison of theoretical and experimental base-pressure ratios.

FIGURE 12.—Concluded. Base flow parameters of pressure-ratio-50 conical nozzle.

of value as an empirical correction to the theoretical limiting-streamline wake-pressure ratio so as to improve the accuracy of predictions of base-pressure ratio. It should be kept in mind, how-

ever, that only approximate methods were used to obtain the free streamline contours, and hence the correlation may not be useful when more exact methods are employed.

In a similar manner, the deviation between theoretical and experimental base pressure is shown in figure 14 as a function of this correlating parameter. The isentropic nozzle types correlated fairly well, but the deviation for the conical nozzle was much less than that of the isentropic nozzles.

HOT-JET MODELS

The base pressure and temperature of the hot-jet models at free-stream Mach numbers of 2.0 and 1.6 are presented in figures 15 to 18. Experimental base-pressure characteristics of the 344 isentropic nozzle are shown in figure 15(a). With the hot-jet models the data were always obtained by increasing the jet-pressure ratio to the desired test value; hence a hysteresis loop, if present, would not have been detected. Experimental

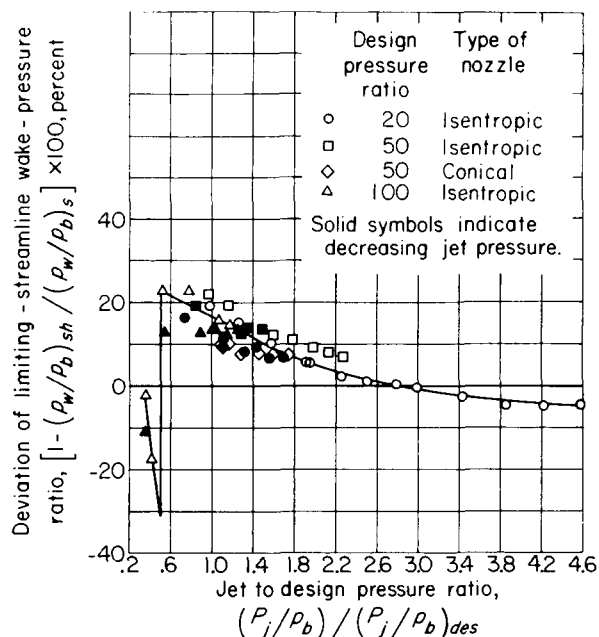


FIGURE 13.—Error correlation for limiting-streamline wake-pressure ratio for cold-jet nozzles.

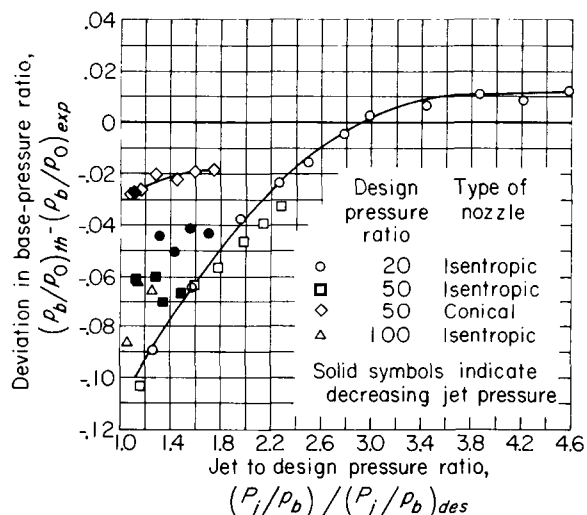


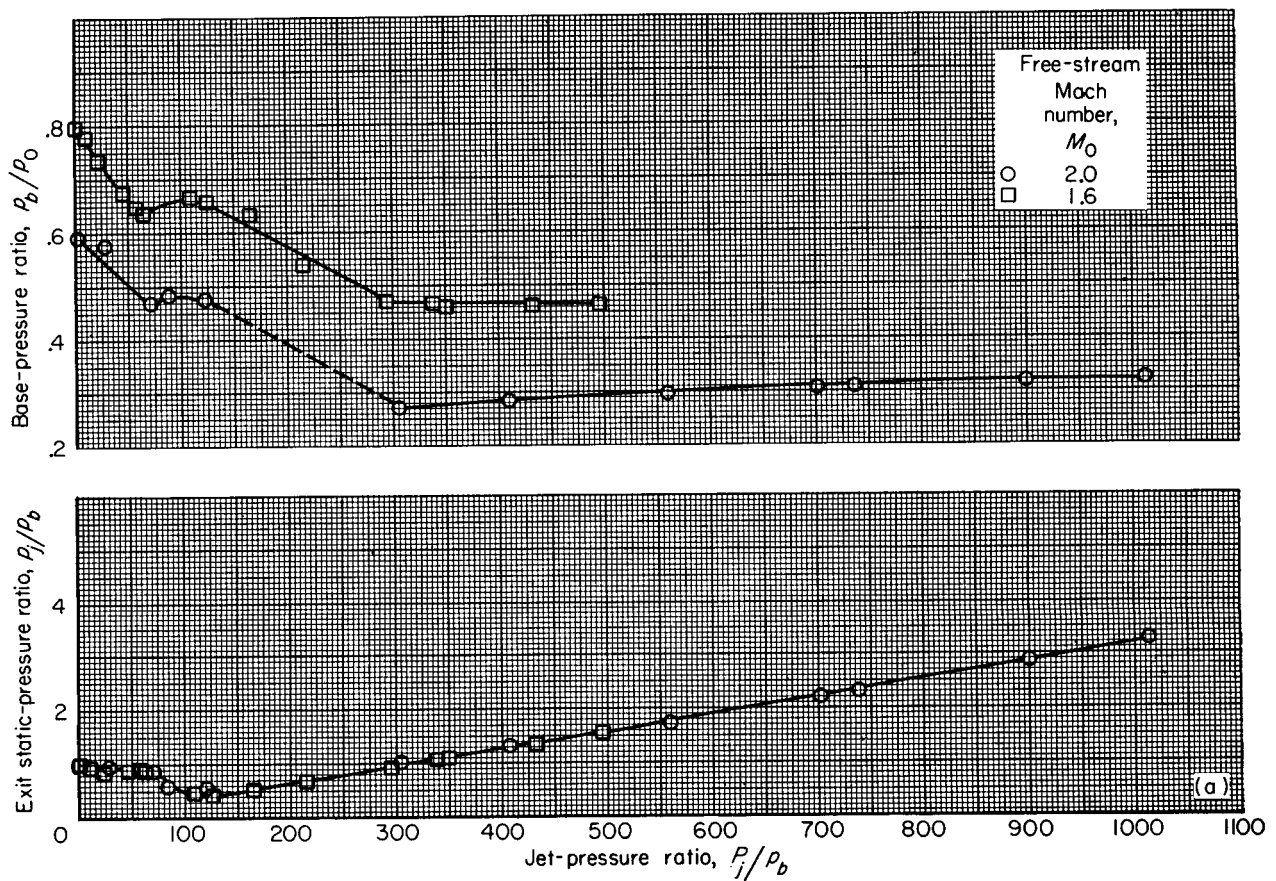
FIGURE 14.—Summary of base-pressure-ratio deviation for cold-jet nozzles.

and theoretical base-pressure ratios of the 344 isentropic nozzle are compared in figures 15(b) and (c) for the two stream Mach numbers. With the hot-jet models this comparison was made only for jet-pressure ratios above design. The theoretical base-pressure ratios were obtained by the method described in appendix B. Since the

jet and stream total temperatures differed, the energy balance described in this appendix was a necessary consideration. (For the cold-jet models, this requirement was automatically satisfied.) For all calculations the external free streamline was obtained from reference 11; the internal free streamline was obtained by one of several methods in the literature. This selection was based on achieving the highest accuracy for the particular nozzle type being studied. For the 344 isentropic nozzle the method of reference 13 was employed. The results in figures 15(b) and (c) show that the theoretical base-pressure ratios were somewhat less than the data at both stream Mach numbers, and that the difference was larger at the lower Mach number.

The experimental base- and jet-temperature ratios (T_b/T_0 and T_j/T_0) and the theoretical base-temperature ratios of the 344 isentropic nozzle are shown in figures 15(d) and (e). At both stream Mach numbers the experimental base temperatures were cooler than theory, and the difference was larger at the higher Mach number. There is a possibility that nozzle wall cooling may have influenced the experimental data so as to produce these cooler base temperatures. The theoretical flow model of appendix B assumes a one-dimensional total-temperature profile at the nozzle exit, whereas in actuality the periphery was cooled an unknown amount by the nozzle wall. Hence the energy terms (particularly $\Omega_{c,i}$) would have been influenced to an unknown extent.

A similar analysis of the base-flow parameters of the 30 isentropic nozzle, the 344 chopped nozzle, and the 30 conical nozzle is presented in figures 16 to 18. Except for the conical nozzle, the internal free streamlines were again obtained by the method of reference 13. For the conical nozzle the characteristic solutions of reference 12 were employed. The comparison between theoretical and experimental base-pressure ratios of the 30 isentropic nozzle (fig. 16(b) and (c)) showed a discrepancy of about the same magnitude as observed for the 344 isentropic nozzle at Mach 2 but less difference at Mach 1.6. However, for the 344 chopped and 30 conical nozzles (figs. 17(b) and (c) and 18(b) and (c)) the theoretical and experimental values were in exceptionally good agreement.



(a) Experimental base-pressure characteristics.

FIGURE 15.—Base-flow parameters of pressure-ratio-344 isentropic nozzle.

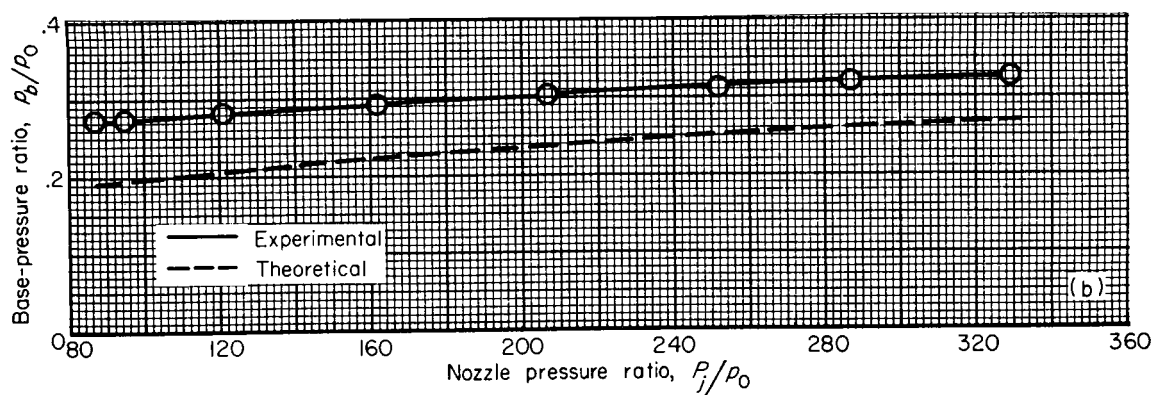
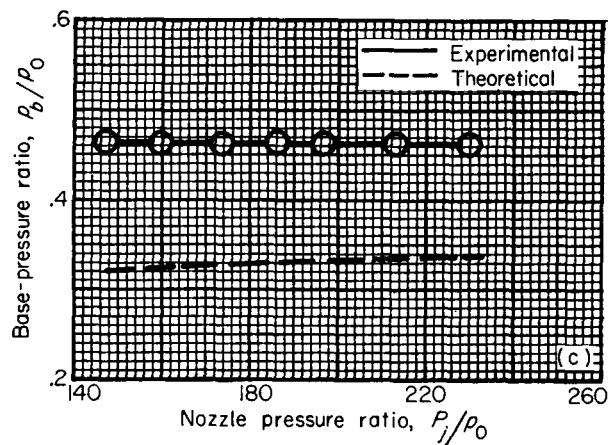
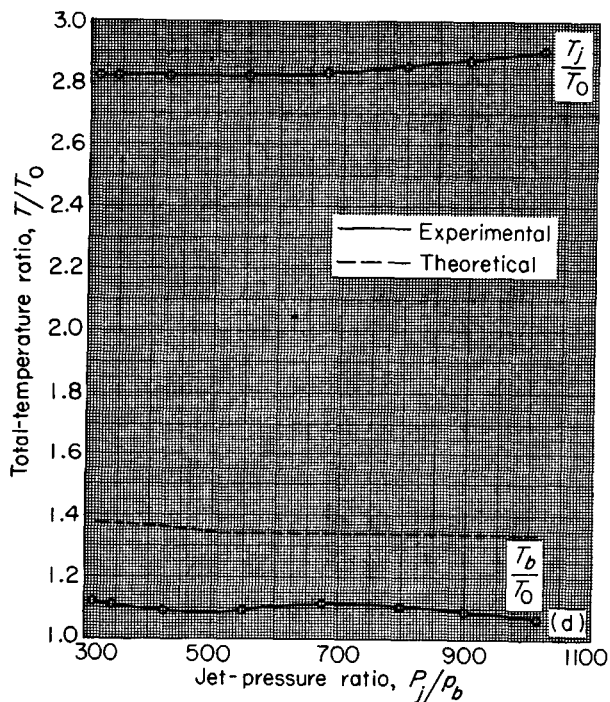
(b) Comparison of theoretical and experimental base-pressure ratios. Free-stream Mach number M_0 , 2.0.

FIGURE 15.—Continued. Base-flow parameters of pressure-ratio-344 isentropic nozzle.



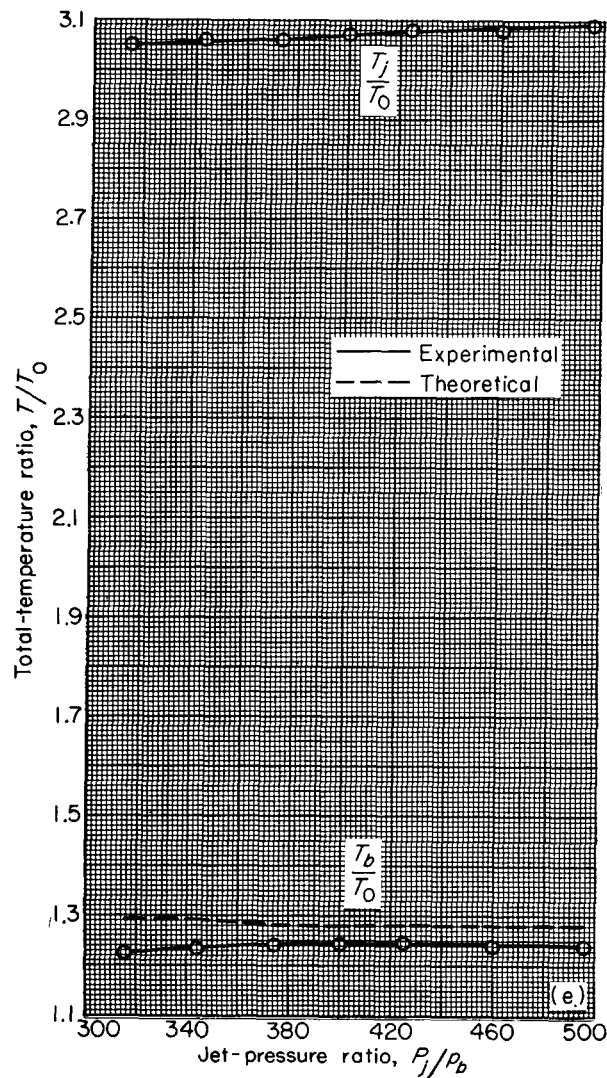
(c) Comparison of theoretical and experimental base-pressure ratios. Free-stream Mach number M_0 , 1.6.

FIGURE 15.—Continued. Base-flow parameters of pressure-ratio-344 isentropic nozzle.



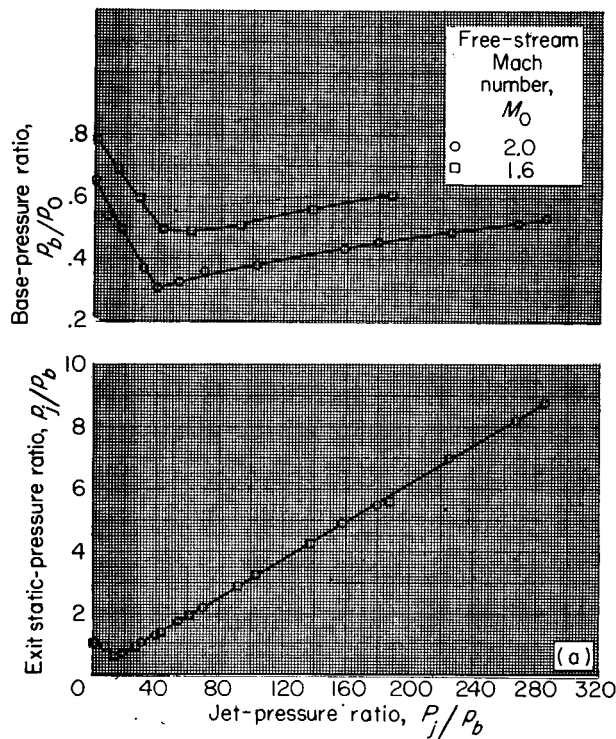
(d) Comparison of theoretical and experimental base-temperature ratios. Free-stream Mach number M_0 , 2.0.

FIGURE 15.—Continued. Base-flow parameters of pressure-ratio-344 isentropic nozzle.



(e) Comparison of theoretical and experimental base-temperature ratios. Free-stream Mach number M_0 , 1.6.

FIGURE 15.—Concluded. Base-flow parameters of pressure-ratio-344 isentropic nozzle.



(a) Experimental base-pressure characteristics.

FIGURE 16.—Base-flow parameters of pressure-ratio-30 isentropic nozzle.

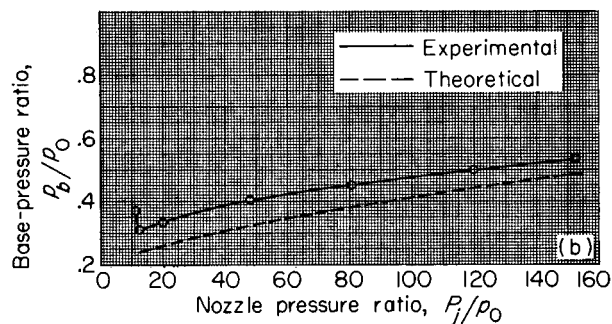
(b) Comparison of theoretical and experimental base-pressure ratios. Free-stream Mach number, M_0 2.0.

FIGURE 16.—Continued. Base-flow parameters of pressure-ratio-30 isentropic nozzle.

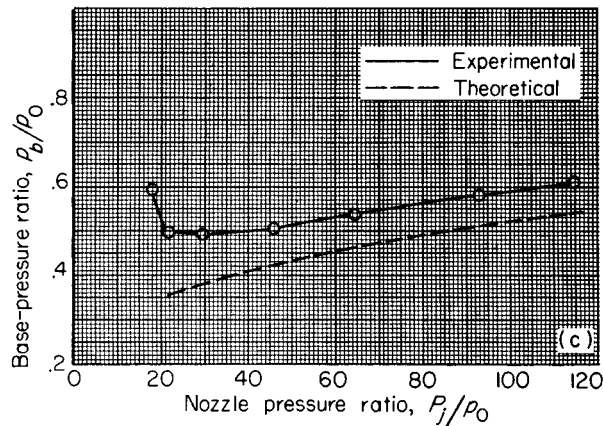
(c) Comparison of theoretical and experimental base-pressure ratios. Free-stream Mach number M_0 1.6.

FIGURE 16.—Continued. Base-flow parameters of pressure-ratio-30 isentropic nozzle.

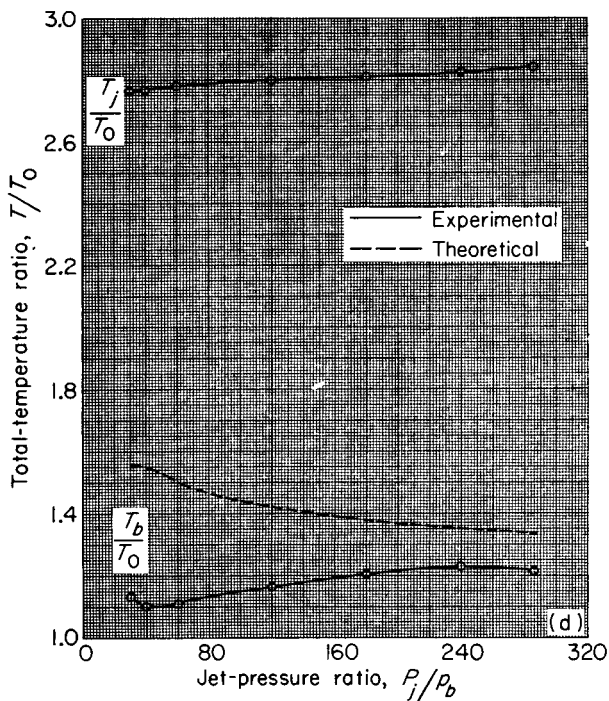
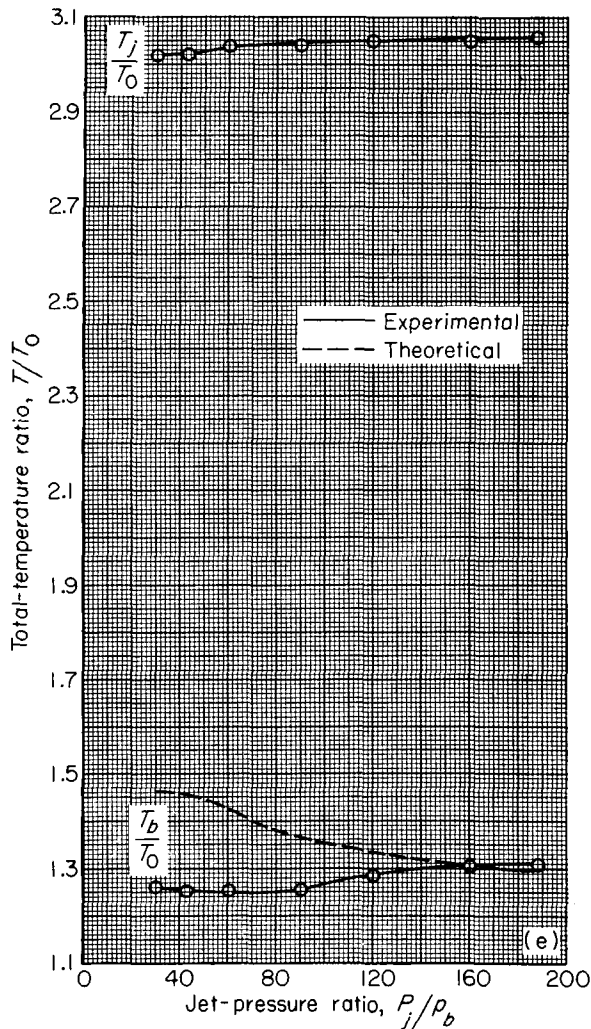
(d) Comparison of theoretical and experimental base-temperature ratios. Free-stream Mach number M_0 2.0.

FIGURE 16.—Continued. Base-flow parameters of pressure-ratio-30 isentropic nozzle.



(e) Comparison of theoretical and experimental base-temperature ratios. Free-stream Mach number M_0 , 1.6.

FIGURE 16.—Concluded. Base-flow parameters of pressure-ratio-30 isentropic nozzle.

The experimental and theoretical base-temperature ratios of these three nozzles (figs. 16(d) and (e), 17(d) and (e), and 18(d) and (e)) showed a trend that had not been observed for the 344 isentropic nozzle: as jet-pressure ratio increased, the differences between theory and experiment decreased. For all the nozzles, however, the experimental values were generally cooler than

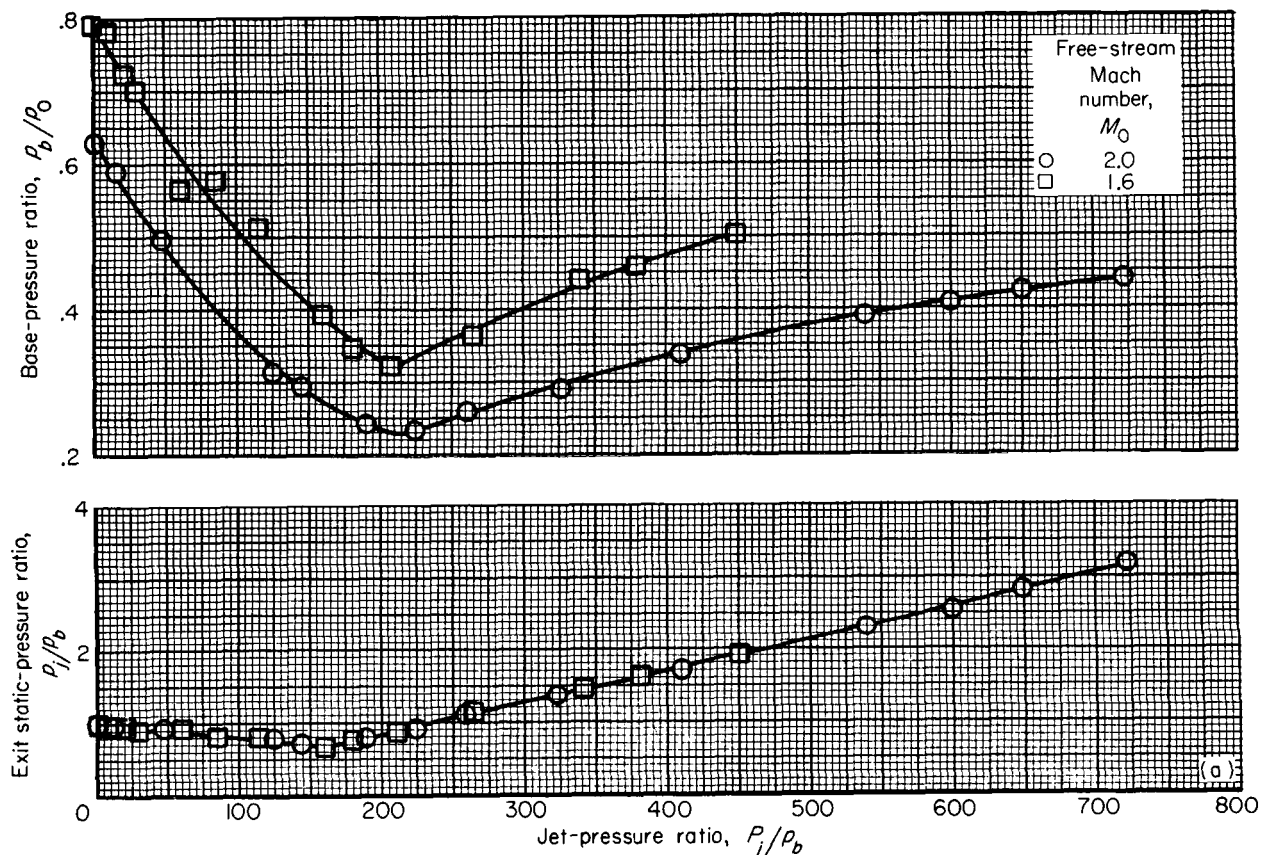
theory, and the discrepancy was larger at the higher free-stream Mach number.

The use of the jet to design pressure ratio as a correlating parameter for the discrepancy between theory and experiment was also investigated for the hot-jet models. Results for the deviation in limiting-streamline wake-pressure ratio are shown in figure 19 for free-stream Mach numbers of 2.0 and 1.6. For purposes of comparison, the cold-jet correlation curve from figure 13 is also shown in figure 19(a). Except for the full-length isentropic nozzles, the results for the hot-jet model did not correlate for the different nozzle designs, nor did they correlate with the cold-jet results. The hot-jet isentropic nozzles correlated well with each other but were at a much higher level than the cold-jet correlation curve. There is a possibility that this lack of correlation may have been a result of inadequacies in determining the internal free streamline. As indicated earlier, different methods were used, depending upon which was most accurate for the particular nozzle design. For all methods, however, there were interpolations, extrapolations, or approximations.

A summary of the deviation between theoretical and experimental base-pressure and -temperature ratios is presented in figures 20 and 21, respectively, as a function of jet to design pressure ratio for both free-stream Mach numbers. The error in base-pressure ratio was less for the short nozzles (the conical and the chopped configurations) than for the full-length isentropic nozzles, and the error in base-temperature ratio generally was less for the high-area-ratio nozzles (the 344 isentropic and the 344 chopped configurations) than for the low-area-ratio designs.

BASE BLEED

Base-bleed effects on base-pressure ratio of the four cold-jet models at a free-stream Mach number of 2.0 are presented in figure 22. Results are presented as a function of bleed mass-flow ratio m_b/m_0 , where m_0 is defined as the free-stream mass-flow rate through an area equal to the annular area of the base. As has been observed in two-dimensional base-bleed studies (e.g., ref.



(a) Experimental base-pressure characteristics.

FIGURE 17.—Base-flow parameters of pressure-ratio-344 chopped nozzle

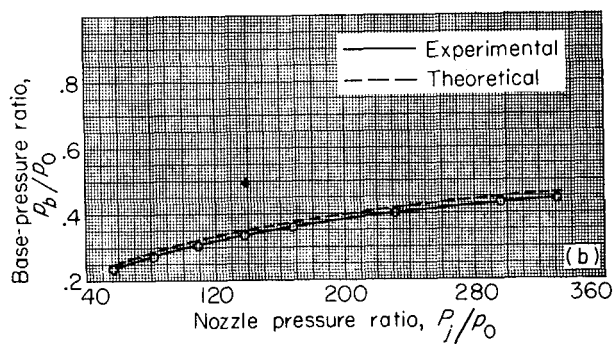
(b) Comparison of theoretical and experimental base-pressure ratios. Free-stream Mach number M_0 , 2.0.

FIGURE 17.—Continued. Base-flow parameters of pressure-ratio-344 chopped nozzle.

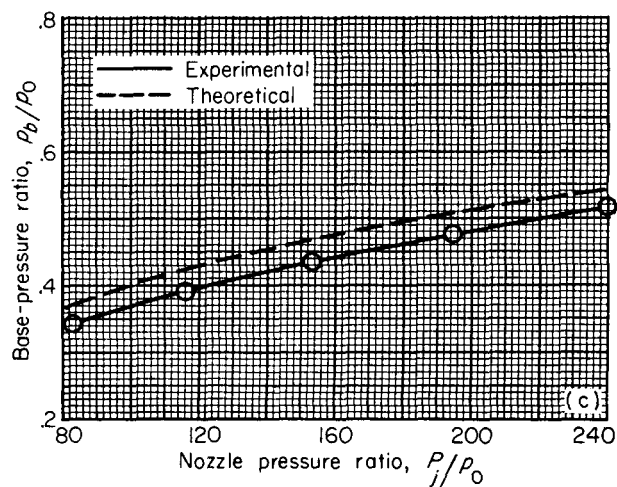
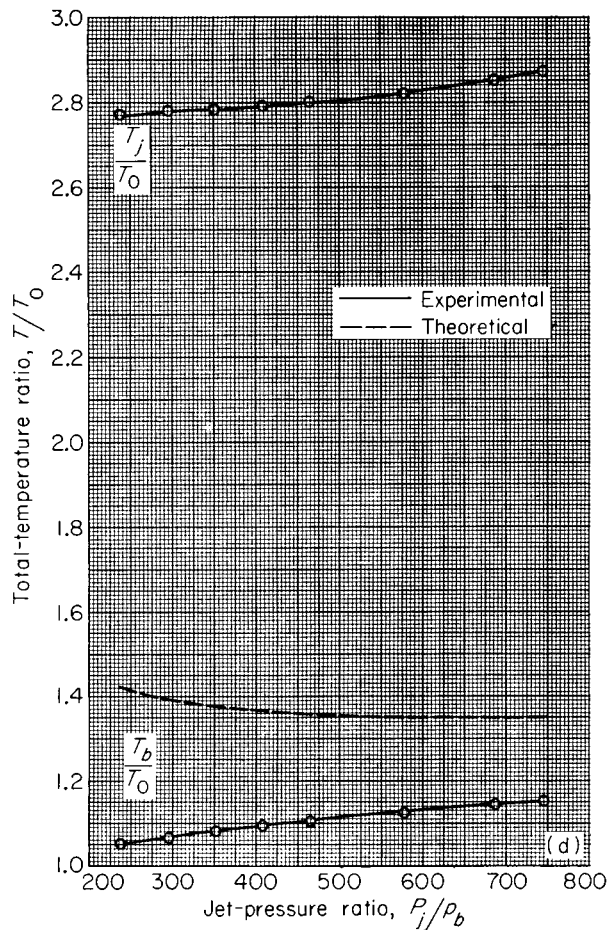
(c) Comparison of theoretical and experimental base-pressure ratios. Free-stream Mach number M_0 , 1.6.

FIGURE 17.—Continued. Base-flow parameters of pressure-ratio-344 chopped nozzle.

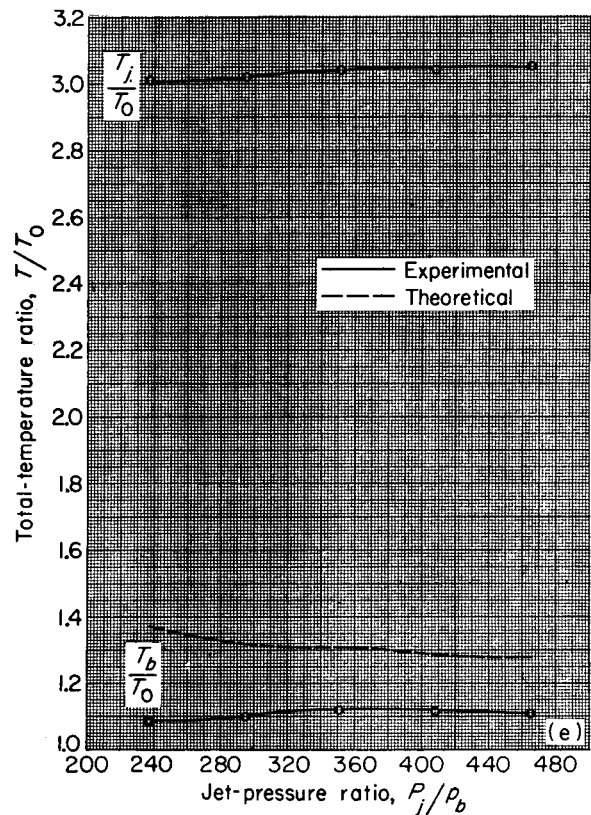


(d) Comparison of theoretical and experimental base-temperature ratios. Free-stream Mach number M_0 , 2.0.

FIGURE 17.—Continued. Base-flow parameters of pressure-ratio-344 chopped nozzle.

14), increasing the bleed-flow rate first increased base-pressure ratio, then decreased it, and finally increased it again. In the range of bleed mass-flow ratios investigated, it is apparent that the base-pressure ratio was virtually independent of nozzle pressure ratio and of nozzle design and was chiefly a function of bleed mass-flow ratio.

These results are further analyzed in figure 23 for the 20 isentropic nozzle, where base-pressure ratio, bleed-pressure ratio P_b/p_0 , and the bleed-flow net-thrust coefficient are shown as functions of the bleed exit Mach number. The base-pressure-ratio curve (fig. 23(a)) shows that the peak in base pressure occurred at a subsonic bleed Mach number of about 0.5 and with a bleed total

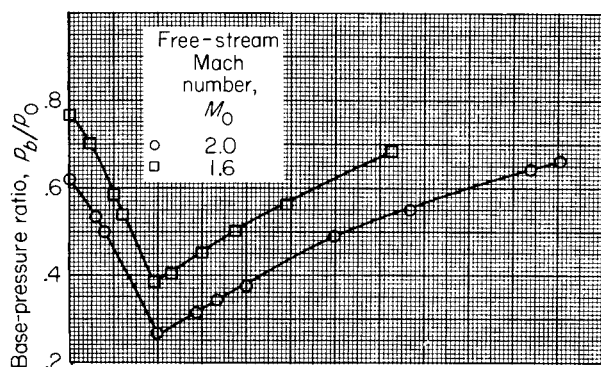


(e) Comparison of theoretical and experimental base-temperature ratios. Free-stream Mach number M_0 , 1.6.

FIGURE 17.—Concluded. Base-flow parameters of pressure-ratio-344 chopped nozzle.

pressure about equal to free-stream static pressure (fig. 23(b)). These results are consistent with the two-dimensional results of reference 14. Figure 23(a) also shows that the minimum base-pressure ratio with base bleed occurred at transonic bleed Mach numbers, and that increases in bleed Mach number into the supersonic range caused a gradual increase in base-pressure ratio.

Two extreme values of bleed-flow net-thrust coefficient are shown in figure 23(c); the maximum value corresponds to the hypothetical situation in which the bleed flow was obtained without an inlet momentum penalty, and the minimum value was obtained by assuming the full free-stream inlet momentum penalty. These results show that, if the bleed flow must be obtained with a free-stream inlet, with the full inlet momentum penalty thereby incurred, there will be no reduction in



(a) Experimental base-pressure characteristics.

FIGURE 18.—Base-flow parameters of pressure-ratio-30 conical nozzle.

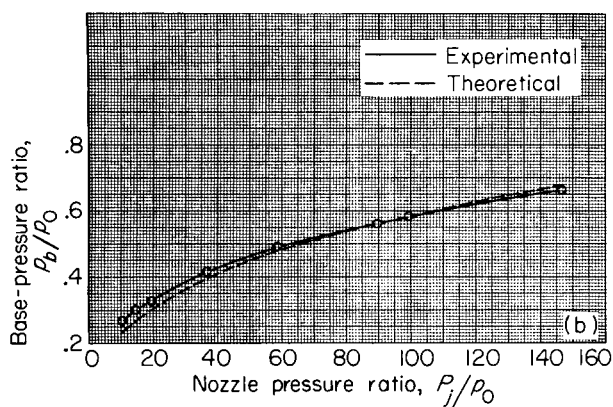
(b) Comparison of theoretical and experimental base-pressure ratios. Free-stream Mach number M_0 , 2.0.

FIGURE 18.—Continued. Base-flow parameters of pressure-ratio-30 conical nozzle.

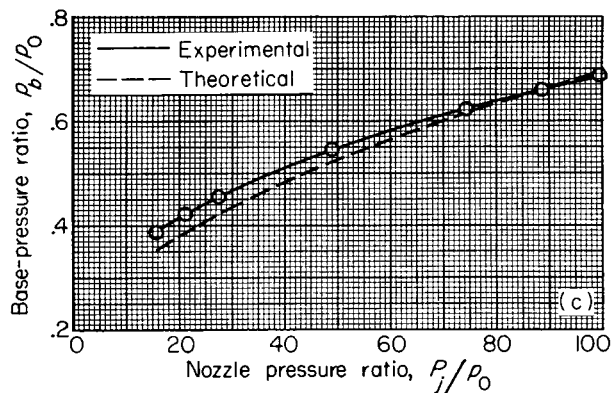
(c) Comparison of theoretical and experimental base-pressure ratios. Free-stream Mach number M_0 , 1.6.

FIGURE 18.—Continued. Base-flow parameters of pressure-ratio-30 conical nozzle.

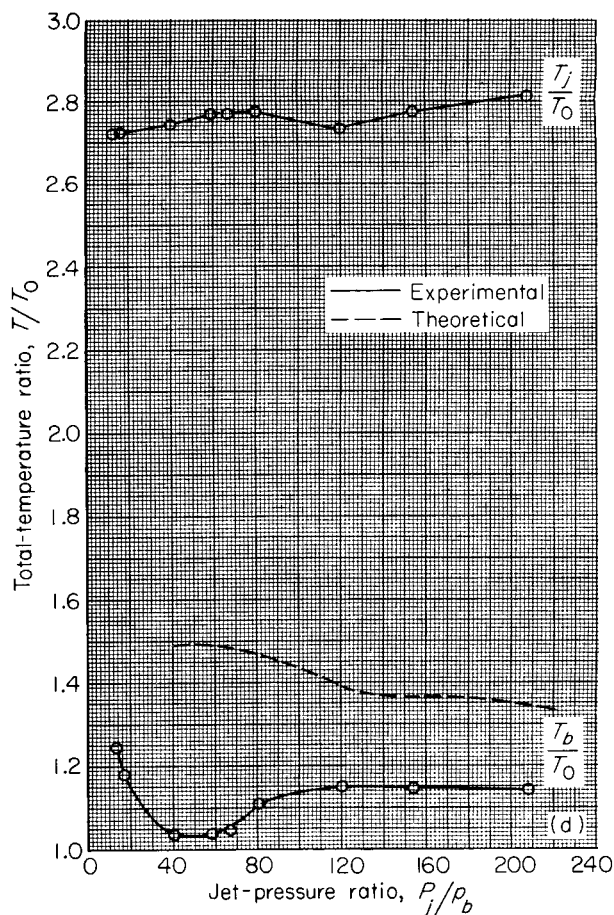
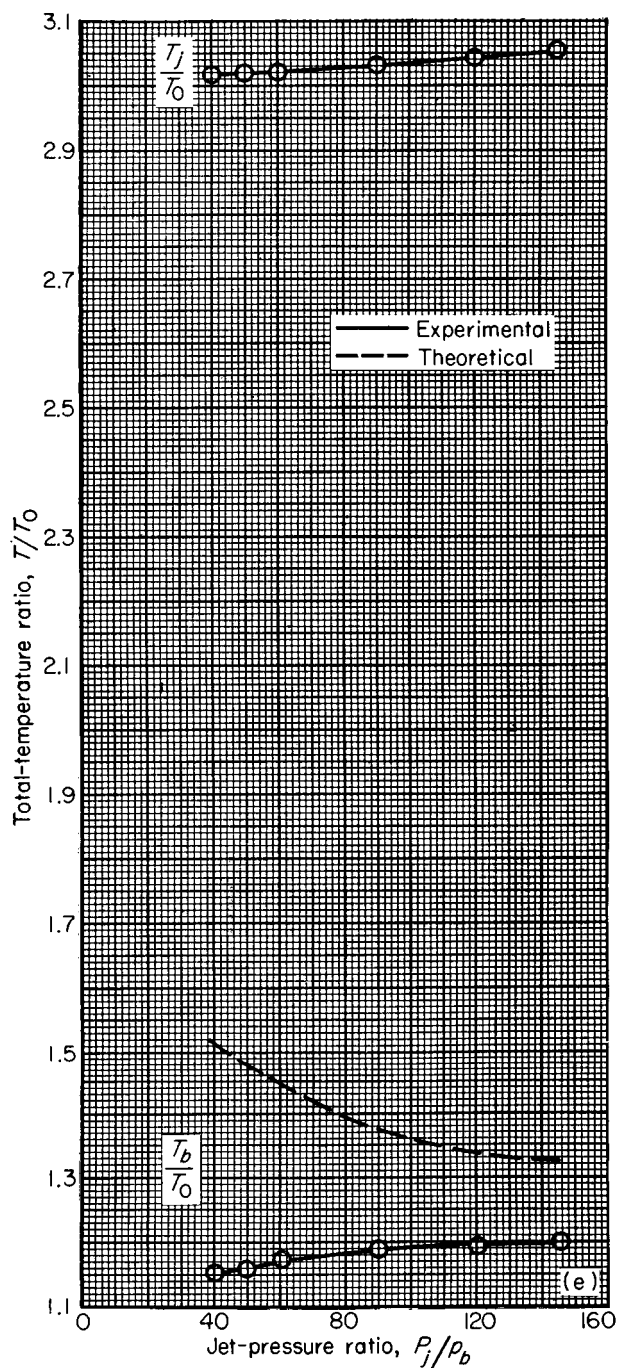
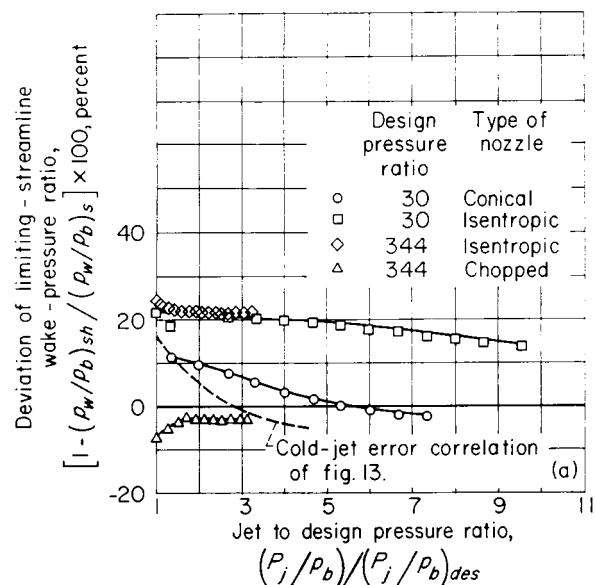
(d) Comparison of theoretical and experimental base-temperature ratios. Free-stream Mach number M_0 , 2.0.

FIGURE 18.—Continued. Base-flow parameters of pressure-ratio-30 conical nozzle.



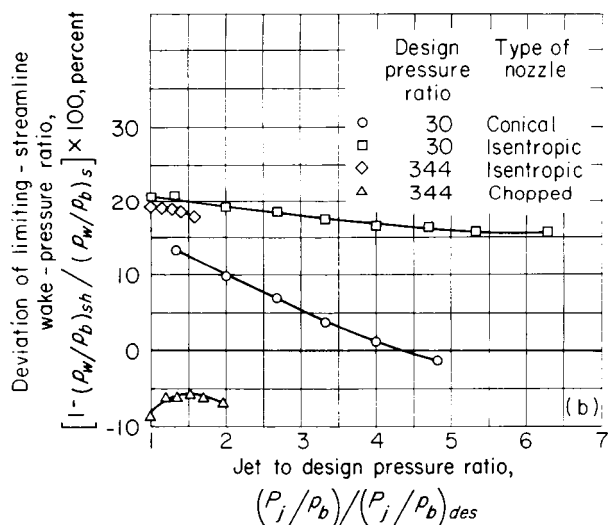
(e) Comparison of theoretical and experimental base-temperature ratios. Free-stream Mach number M_0 , 1.6.

FIGURE 18.—Concluded. Base-flow parameters of pressure-ratio-30 conical nozzle.



(a) Free-stream Mach number M_0 , 2.0.

FIGURE 19.—Error correlation for limiting-streamline wake-pressure ratio for hot-jet nozzles.



(b) Free-stream Mach number M_0 , 1.6.

FIGURE 19.—Concluded. Error correlation for limiting-streamline wake-pressure ratio for hot-jet nozzles.

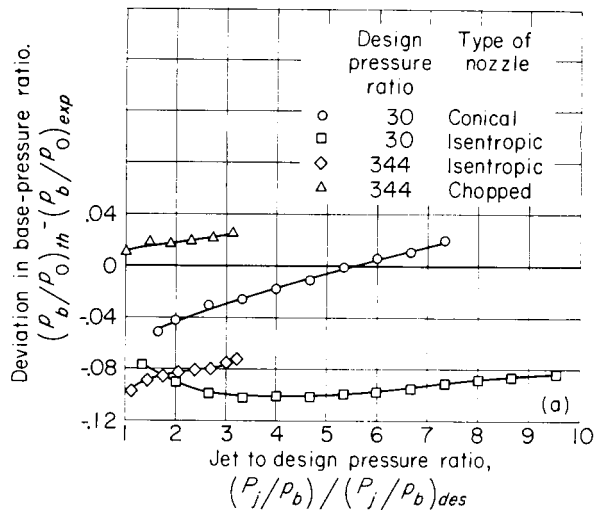
(a) Free-stream Mach number M_0 , 20.

FIGURE 20.—Summary of base-pressure-ratio deviation for hot-jet nozzles.

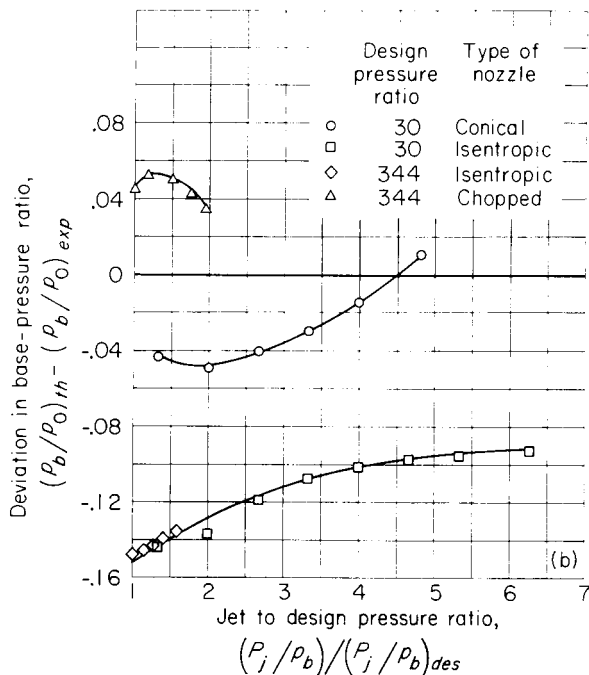
(b) Free-stream Mach number M_0 , 1.6.

FIGURE 20.—Concluded. Summary of base-pressure-ratio deviation for hot-jet nozzles.

net base drag. However, if the bleed inlet can be located so as to reduce the inlet momentum penalty (e.g., in the boundary layer of another surface), there is a possibility of improving the overall performance. The actual performance

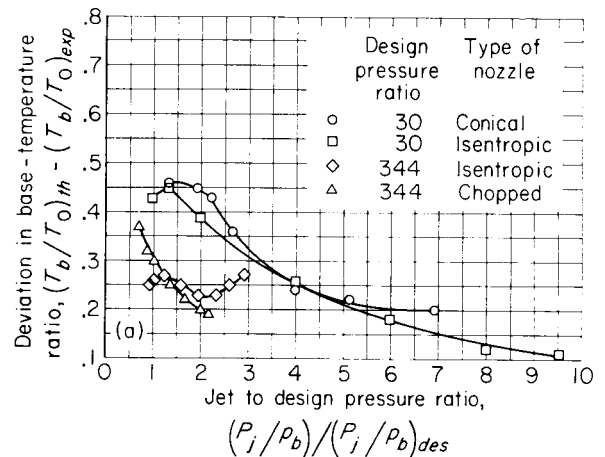
(a) Free-stream Mach number M_0 , 2.0.

FIGURE 21.—Summary of base-temperature-ratio deviation.

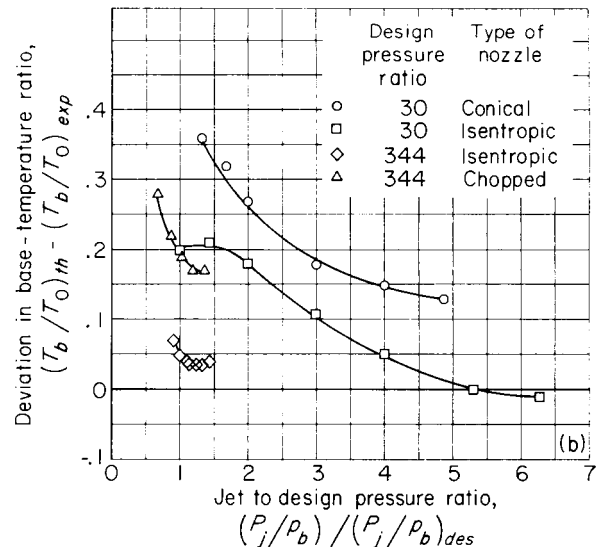
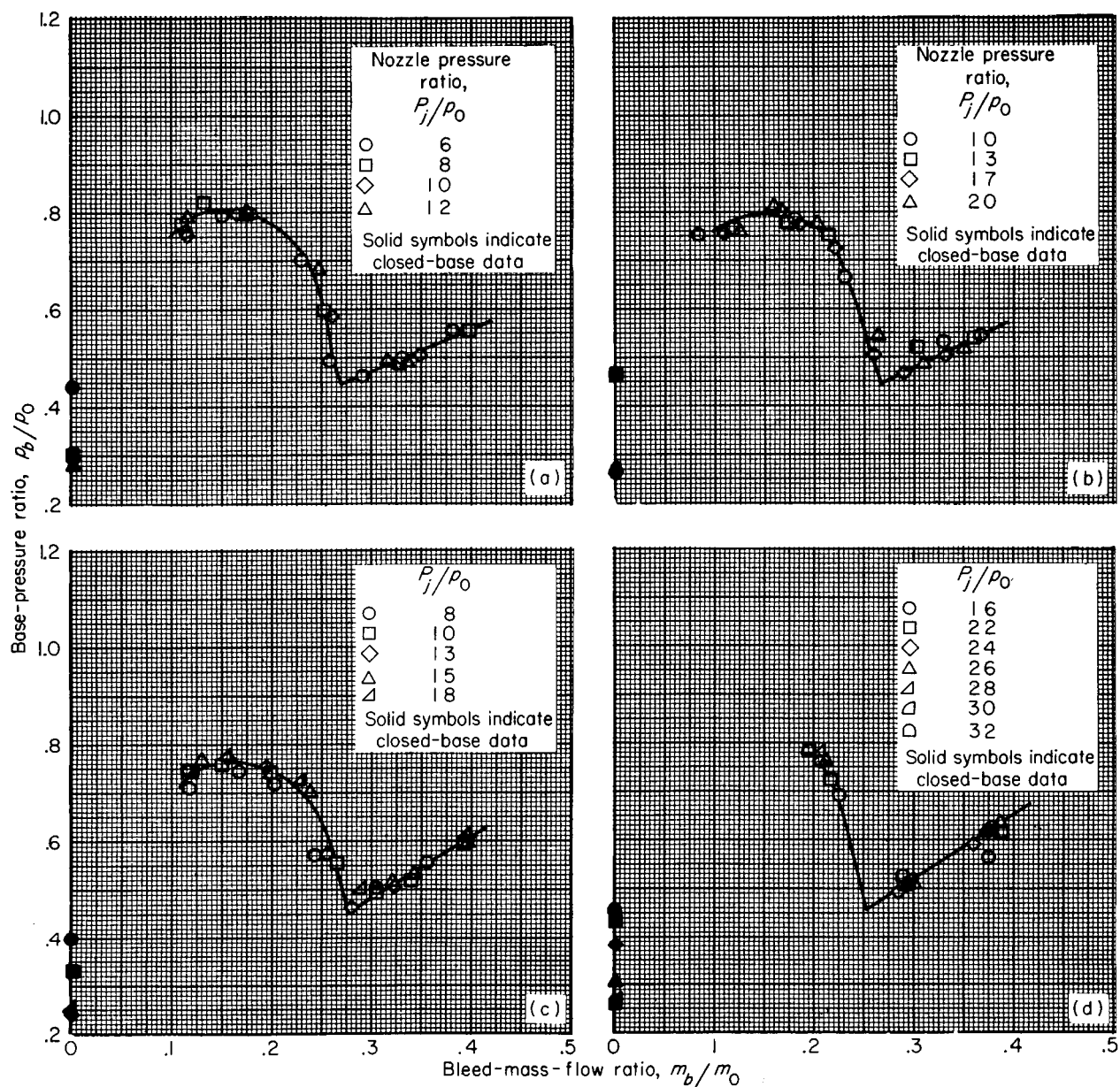
(b) Free-stream Mach number M_0 , 1.6.

FIGURE 21.—Concluded. Summary of base-temperature-ratio deviation.

then would lie somewhere between the curves of maximum and minimum thrust coefficient, the location depending upon the particular installation.

The calculation procedure of appendix B was used to determine the theoretical effects of base bleed on base pressure. A typical solution is shown in figure 24(a) for the 20 isentropic nozzle at a nozzle pressure ratio of 12.2. As described earlier in figure 9(c), several values of base-pressure ratio are assumed, and the corresponding



(a) Pressure-ratio-20 isentropic nozzle.

(b) Pressure-ratio-50 isentropic nozzle.

(c) Pressure-ratio-50 conical nozzle.

(d) Pressure-ratio-100 isentropic nozzle.

FIGURE 22.—Effect of base bleed on base-pressure ratio for cold-jet models.

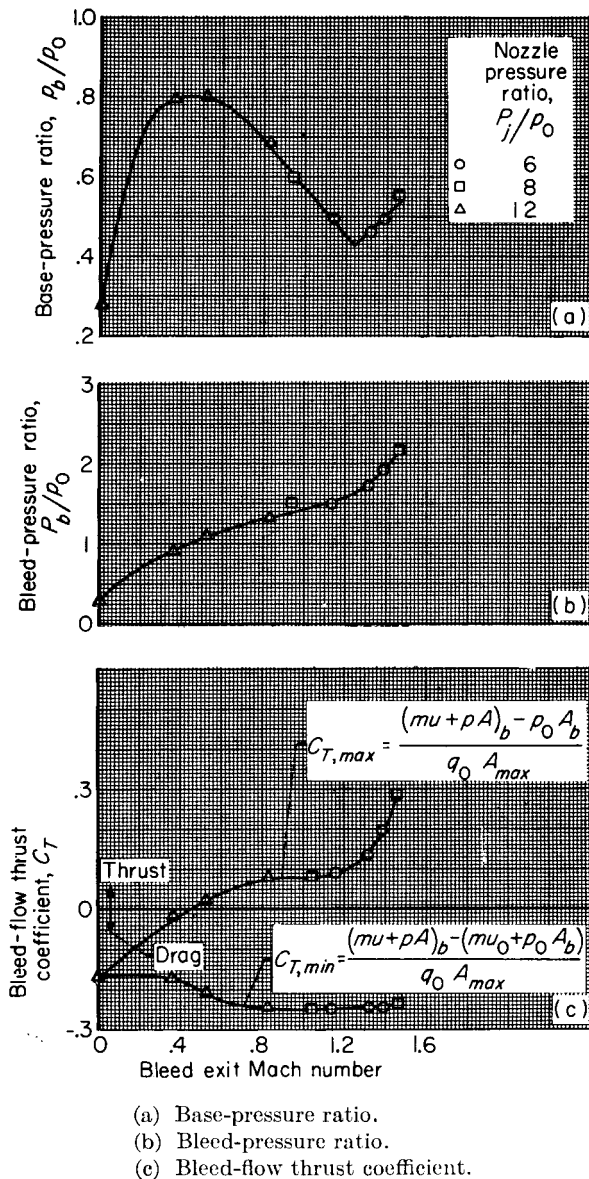
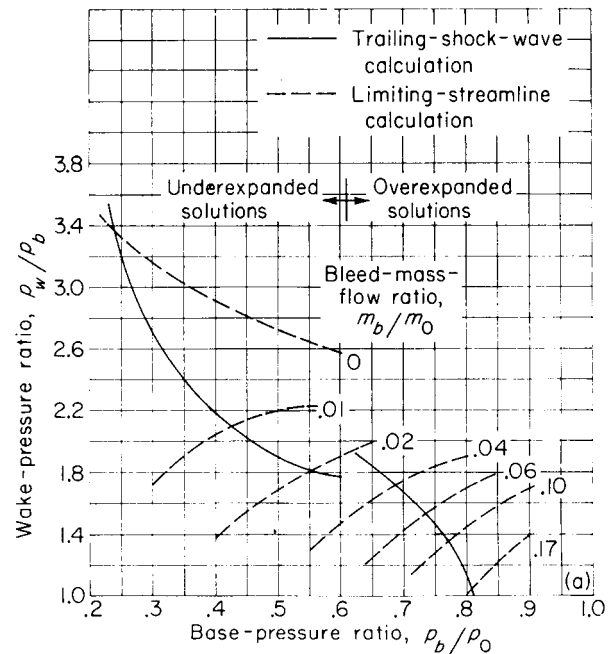


FIGURE 23.—Analysis of base-bleed performance for pressure-ratio-20 isentropic nozzle.

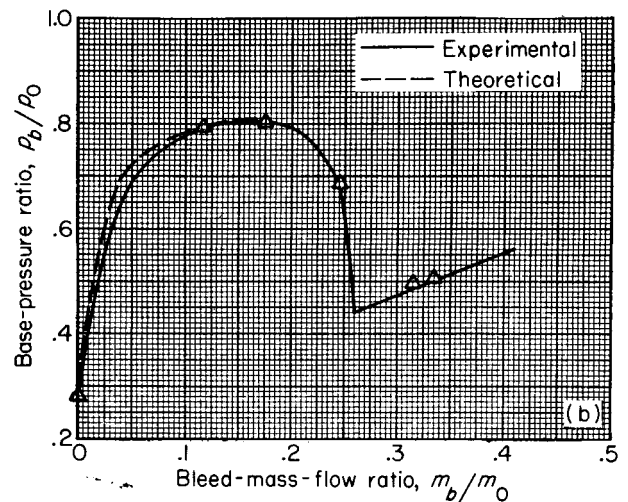
values of trailing-shock and limiting-streamline pressure rise are determined. Since the limiting-streamline wake-pressure ratio depends upon base-bleed mass-flow ratio, several values were assumed. The base-pressure solution then for a given value of bleed-flow ratio is that base-pressure ratio for which the trailing-shock and the appropriate limiting-streamline wake-pressure ratios are equal.

A comparison of theoretical and experimental base-bleed effect is shown in figure 24(b). The



(a) Theoretical solutions. Nozzle pressure ratio P_i/p_0 , 12.2.

FIGURE 24.—Prediction of base-bleed effects on base-pressure-ratio for pressure-ratio-20 isentropic nozzle.



(b) Comparison with experimental data.

FIGURE 24.—Concluded. Prediction of base-bleed effects on base-pressure ratio for pressure-ratio-20 isentropic nozzle.

results show excellent agreement in the range of low bleed-flow ratios for which base-pressure ratio was increasing to the peak value. At higher bleed-flow rates the experimental base pressures decreased because of effects of the bleed axial momentum (ref. 15). Since this effect was neglected in the theoretical calculations, the analysis was inadequate for the high bleed-flow rates.

SUMMARY OF RESULTS

A theoretical and experimental investigation of jet-stream interaction effects on annular base pressure and temperature has been conducted. Eight single-jet nozzle configurations of varying design were studied. Four of these used unheated air as the propellant fluid and were investigated at a free-stream Mach number of 2.0; the others employed a hydrogen peroxide rocket system and were investigated at Mach 2.0 and 1.6. Results were as follows:

1. Temperature and velocity distributions in

the flow downstream of the base showed qualitative agreement with the theoretical flow model.

2. For jet-pressure ratios equal to or greater than design, predicted base-pressure ratios were generally less than experimental values and were in closer agreement with the conical and shortened isentropic nozzles than with the full-length isentropic nozzles.

3. In general the predicted base-temperature ratios were greater than the experimental values, and the deviation decreased with increasing jet-pressure ratio. This deviation was less at Mach 1.6 than at 2.0 and was less for high-area-ratio nozzles than for low-area-ratio designs.

4. The effect of base bleed on base-pressure ratio could be predicted with good accuracy in the range of bleed flows for which the bleed momentum could be neglected.

LEWIS RESEARCH CENTER

NATIONAL AERONAUTICS AND SPACE ADMINISTRATION
CLEVELAND, OHIO, *June 21, 1961*

APPENDIX A

SYMBOLS

A	area	η	position parameter, $\sigma \frac{y}{x}$
A_{max}	maximum model cross-sectional area	ρ	density
C	Crocco number	σ	similarity parameter, $12 + 2.758 M$
C_T	net-thrust coefficient	φ	mixing-profile velocity ratio, local velocity/ velocity outside mixing profile
c_p	specific heat at constant pressure	Ω	energy transfer rate
D	diameter	Subscripts:	
E	energy function (see appendix B)	b	base or bleed
erf	error function $\left(erf \ \eta = \frac{2}{\sqrt{\pi}} \int_0^\eta e^{-\beta^2} d\beta \right)$	c	conductive
G	mass-flow function (see appendix B)	d	convective
M	Mach number	des	design
m	mass-flow rate	e	external flow
m_0	equivalent free-stream mass-flow rate through open base, $\rho_0 u_0 A_b$	exp	experimental
P	total pressure	i	internal flow
p	static pressure	j	jet exit or separating streamline
q	dynamic pressure	l	local
R	gas constant	max	maximum
r	radial distance	min	minimum
T	total temperature	r	reflected (see fig. 1(b))
t	static temperature	ref	reference
u	velocity	s	nozzle wall surface or limiting streamline
X	mixing-length ratio, $(x_i/\sigma_i)/(x_e/\sigma_e)$	sh	shock
x	length of streamline from base to trailing shock or abscissa of mixing-profile coordi- nates	th	theory
y	ordinate of mixing-profile coordinates	w	wake
Z	axial distance	0	free stream
β	dummy variable	Superscripts:	
γ	specific-heat ratio	$*$	sonic
		$-$	per unit width at origin of trailing-shock waves

APPENDIX B

THEORETICAL CALCULATION OF BASE-PRESSURE RATIO p_b/p_0 AND BASE-GAS-TEMPERATURE RATIO T_b/T_0

For a given base configuration it was assumed that all geometric parameters were known and that certain flow parameters were specified just upstream of the base surface for both the internal (jet) and external (free-stream) flow. These parameters are indicated in figure 1(a) and included: Mach numbers M_0 and M_j just outside the surface boundary layers; static pressures p_0 and p_j at the afterbody surface and nozzle wall, respectively; total temperatures T_0 and T_j , which were assumed to be uniform in each of the two streams (thus heat-transfer effects to the afterbody external surface and to the nozzle wall were neglected); and gas properties γ and R of both streams, which were assumed to be in frozen equilibrium at all stations downstream of the base surface (thus effects of recombination were neglected). In addition a base-bleed flow rate and a base-energy-addition rate were allowed in the analysis. (Energy addition could result from base burning, heat transfer through the base surface, etc.) The theoretical base pressure and base gas temperature were computed by the following steps:

(1) A value of base-pressure ratio p_b/p_0 was assumed.

(2) The resulting value of the trailing-shock pressure ratio p_w/p_b was determined. This was accomplished by first determining the flow directions and Mach numbers of the internal and external free streamlines just upstream of their intersection (neglecting effects of mixing) by one of several methods in the literature for axisymmetric flows. Modifications to these methods were required to approximate the jet shape for overexpanded jet flow. It was assumed that the static pressure along the free streamlines was constant and equal to p_b from the base surface to the point of their intersection. The trailing-shock pressure ratio then was that corresponding to a plane shock wave in both the internal and

external flows which produced parallel flow with uniform static pressure p_w downstream of the waves.

(3) The stagnation-pressure rise of the limiting streamline and the base-gas-temperature ratio T_b/T_0 that corresponded to the assumed value of base-pressure ratio were then determined.

(a) A value of base-gas-temperature ratio $\frac{T_b}{T_0} \left(= \frac{T_b}{T_e} \right)$ was assumed.

(b) The corresponding gas properties γ and R of the base gas were computed. For this calculation it was assumed that the base-bleed gas, if any, had the same gas properties and total temperature as either the internal or external flow. As in reference 6 it was further assumed that the total-temperature spread during the mixing process was the same as that of momentum, and hence the total-temperature profile across the mixing zone was similar to the velocity profile

expressed by $\varphi = \frac{1}{2}(1 + \operatorname{erf} \eta)$. In the present

analysis the additional assumption was made that gas concentration also spread at the same rate as momentum, and hence that gas properties varied linearly with total temperature across the mixing zones. Hence base gas properties were computed from the following equations:

$$\gamma_b = \gamma_e + \frac{\gamma_i - \gamma_e}{\frac{T_i}{T_e} - 1} \left(\frac{T_b}{T_e} - 1 \right)$$

and

$$R_b = R_e + \frac{R_i - R_e}{\frac{T_i}{T_e} - 1} \left(\frac{T_b}{T_e} - 1 \right)$$

(c) Several locations of the external limiting streamline $\eta_{s,e}$ were assumed.

(d) For each value of $\eta_{s,e}$ the isentropic stag-

nation-pressure ratio of that streamline was computed. To accomplish this, it was necessary to determine the gas properties and Mach number along that streamline. Since gas properties were assumed to vary linearly with velocity ratio φ , the following relations were used to determine them at any local point l within the profile: for the external flow $\gamma_l = \gamma_b + (\gamma_e - \gamma_b)\varphi_l$ and $R_l = R_b + (R_e - R_b)\varphi_l$, and for the internal flow $\gamma_l = \gamma_b + (\gamma_i - \gamma_b)\varphi_l$ and $R_l = R_b + (R_i - R_b)\varphi_l$. To determine the Mach number of these streamlines, it was necessary first to determine the static-temperature variation through the mixing region. At any local point in the external mixing profile $\frac{t_l}{t_e} = \left(\frac{t_l}{T_l}\right)\left(\frac{T_l}{T_e}\right)\left(\frac{T_e}{t_e}\right)$. By use of the Crocco number C (which is related to Mach number by the equation $\frac{C^2}{1-C^2} = \frac{\gamma-1}{2} M^2$), the static-temperature ratio may be written as

$$\frac{t_l}{t_e} = \frac{1 - \frac{c_{p,e}}{c_{p,l}} \varphi_l^2 C_e^2}{1 - C_e^2} + \frac{\left(\frac{T_b}{T_e} - 1\right)(1 - \varphi_l)}{1 - C_e^2}$$

Similarly for the internal flow

$$\frac{t_l}{t_i} = \frac{1 - \frac{c_{p,i}}{c_{p,l}} \varphi_l^2 C_i^2}{1 - C_i^2} + \frac{\left(\frac{T_b}{T_i} - 1\right)(1 - \varphi_l)}{1 - C_i^2}$$

In each equation the ratio of specific heats was required; that is, $\frac{c_{p,e}}{c_{p,l}}$ and $\frac{c_{p,i}}{c_{p,l}}$. In a manner similar to that used to obtain the other gas properties, these ratios were computed from

$$\frac{c_{p,e}}{c_{p,l}} = \frac{c_{p,e}}{c_{p,b}} + \left(1 - \frac{c_{p,e}}{c_{p,b}}\right) \varphi_l \text{ and } \frac{c_{p,i}}{c_{p,l}} = \frac{c_{p,i}}{c_{p,b}} + \left(1 - \frac{c_{p,i}}{c_{p,b}}\right) \varphi_l$$

for the external and internal flows, respectively. (The values of $c_{p,e}$ and $c_{p,i}$ are known of course from the relation $c_p = \frac{\gamma R}{\gamma - 1}$.)

The Mach number along each of the assumed external limiting streamlines was computed from the equation

$$M_{s,e} = \frac{\varphi_{s,e} M_e}{\sqrt{\frac{\gamma_{s,e} R_{s,e}}{\gamma_e R_e} \frac{t_{s,e}}{t_e}}} =$$

and the isentropic stagnation-pressure ratio was computed from

$$\left(\frac{P}{p}\right)_{s,e} = \left(1 + \frac{\gamma_{s,e} - 1}{2} M_{s,e}^2\right)^{\frac{\gamma_{s,e}}{\gamma_{s,e} - 1}}$$

(e) For each assumed location of the external limiting streamline, the location of the internal limiting streamline $\eta_{s,i}$ that had the same stagnation-pressure ratio was determined. This was accomplished by trial-and-error assumptions of $\eta_{s,i}$ and by computing the stagnation-pressure ratio for each assumed value in a manner identical to that described previously for the external limiting streamline. The following equations were used:

$$\gamma_{s,i} = \gamma_b + (\gamma_i - \gamma_b) \varphi_{s,i}$$

$$R_{s,i} = R_b + (R_i - R_b) \varphi_{s,i}$$

$$M_{s,i} = \frac{\varphi_{s,i} M_i}{\sqrt{\frac{\gamma_{s,i} R_{s,i}}{\gamma_i R_i} \frac{t_{s,i}}{t_i}}} =$$

$$\left(\frac{P}{p}\right)_{s,i} = \left(1 + \frac{\gamma_{s,i} - 1}{2} M_{s,i}^2\right)^{\frac{\gamma_{s,i}}{\gamma_{s,i} - 1}}$$

Hence for each value of $\eta_{s,e}$ there was a corresponding value of $\eta_{s,i}$ such that $\left(\frac{P}{p}\right)_{s,e} = \left(\frac{P}{p}\right)_{s,i}$.

(f) The mass-flow balance of the base region was analyzed next. The fundamental equation for this analysis was, as indicated in figure 1(c), $m_{s,e} + m_{s,i} + m_b = \Delta m$, where $m_{s,e}$ and $m_{s,i}$ refer to the integrated mass-flow rates between the separating and the limiting streamlines of the external and the internal flows, respectively, and m_b is the base-bleed-flow rate. A requirement of the solution then was to determine values of the unknowns T_b/T_e and $\eta_{s,e}$ such that Δm was zero. However, for arbitrary choices of these values, Δm was not zero and therefore was evaluated for each of the values chosen in steps (3) (a) and (c).

The mass-flow rate per unit width between the limiting and separating streamlines was determined at the origin of the trailing-shock waves from the following equations (neglecting three-dimensional effects in the integrations) for the external and internal flows, respectively:

$$\bar{m}_{s,e} = \int_{y_{i,e}}^{y_{s,e}} \rho u_i \gamma_e = \frac{x_e}{\sigma_e} \rho_e u_e R_e$$

$$\left(\int_{-\infty}^{\eta_{ref}} \frac{\varphi^2}{R \frac{t}{t_e}} d\eta - \int_{\eta_{s,e}}^{\eta_{ref}} \frac{\varphi}{R \frac{t}{t_e}} d\eta \right)$$

and

$$\bar{m}_{s,i} = \int_{y_{j,i}}^{y_{s,i}} \rho u_i dy = \frac{x_i}{\sigma_i} \rho_i u_i R_i$$

$$\left(\int_{-\infty}^{\eta_{ref}} \frac{\varphi^2}{R \frac{t}{t_i}} d\eta - \int_{\eta_{s,i}}^{\eta_{ref}} \frac{\varphi}{R \frac{t}{t_i}} d\eta \right)$$

These equations were similar to those derived in reference 6 with the exception that R was treated as a variable in the integration and was approximated in the present analysis by $R = R_b + (R_e - R_b)\varphi$ for the external flow and by $R = R_b + (R_i - R_b)\varphi$ for the internal flow.

The mass-flow balance equation could then be written as

$$\Delta G \equiv \frac{\Delta \bar{m} \sigma_e \gamma_e T_i}{x_e \rho_b \gamma_e R_e} = \left(\frac{\bar{m}_b \sigma_e \gamma_e T_i}{x_e \rho_b \gamma_e R_e} \right) + \left(\frac{\bar{m}_{s,e} \sigma_e}{x_e \rho_e u_e R_e} \right) \frac{M_e}{\sqrt{\left(\frac{T_e}{T_i} \right) \left(\frac{t_e}{T_i} \right)}}$$

$$+ \left(\frac{\bar{m}_{s,i} \sigma_i}{x_i \rho_i u_i R_i} \right) \frac{x_i}{\sigma_e} \frac{M_i}{\sqrt{\frac{\gamma_e R_i}{\gamma_e \gamma_e} \frac{t_i}{T_i}}}$$

and was evaluated for each value of T_b/T_e and $\eta_{s,e}$.

(g) In a similar manner (again neglecting three-dimensional effects in the integrations) the energy balance of the base region was analyzed. As indicated in figure 1(d), the energy-transfer processes were due to a convective flux between the separating and limiting streamlines of the internal and external flows, a conductive flux through the mixing regions normal to the velocities, and heat addition (or subtraction) to the base region from an external source. The energy

balance may be written as $\Omega_{d,e} + \Omega_{d,i} + \Omega_{c,e} + \Omega_{c,i} + \Omega_b = \Delta \Omega$. Thus an additional restriction on the values of the unknowns T_b/T_e and $\eta_{s,e}$ was that $\Delta \Omega = 0$. As with the continuity equation discussed earlier, an arbitrary choice of these values does not satisfy this requirement, and hence $\Delta \Omega$ was evaluated for each of the assumed values.

In calculating the convective terms it was necessary to locate the external and internal separating streamlines $\eta_{j,e}$ and $\eta_{j,i}$. They were determined from the equations:

$$\int_{\eta_{j,e}}^{\eta_{ref}} \frac{\varphi}{R \frac{t}{t_e}} d\eta = \int_{-\infty}^{\eta_{ref}} \frac{\varphi^2}{R \frac{t}{t_e}} d\eta$$

and

$$\int_{\eta_{j,i}}^{\eta_{ref}} \frac{\varphi}{R \frac{t}{t_i}} d\eta = \int_{-\infty}^{\eta_{ref}} \frac{\varphi^2}{R \frac{t}{t_i}} d\eta$$

The convective terms were then evaluated as follows:

$$\bar{\Omega}_{d,e} = \int_{y_{j,e}}^{y_{s,e}} \rho u c_p T dy = \frac{x_e}{\sigma_e} \rho_e u_e R_e T_e$$

$$\left[\frac{T_b}{T_e} \int_{\eta_{j,e}}^{\eta_{s,e}} \frac{\gamma}{\gamma-1} \frac{\varphi}{t_e} d\eta + \left(1 - \frac{T_b}{T_e} \right) \int_{\eta_{j,e}}^{\eta_{s,e}} \frac{\gamma}{\gamma-1} \frac{\varphi^2}{t_e} d\eta \right]$$

and

$$\bar{\Omega}_{d,i} = \int_{y_{j,i}}^{y_{s,i}} \rho u c_p T dy = \frac{x_i}{\sigma_i} \rho_i u_i R_i T_i$$

$$\left[\frac{T_b}{T_i} \int_{\eta_{j,i}}^{\eta_{s,i}} \frac{\gamma}{\gamma-1} \frac{\varphi}{t_i} d\eta + \left(1 - \frac{T_b}{T_i} \right) \int_{\eta_{j,i}}^{\eta_{s,i}} \frac{\gamma}{\gamma-1} \frac{\varphi^2}{t_i} d\eta \right]$$

where $\gamma = \gamma_b + (\gamma_e - \gamma_b)\varphi$ for the external flow and $\gamma = \gamma_b + (\gamma_i - \gamma_b)\varphi$ for the internal flow. These equations and their derivations are also similar to those of reference 6 with the exception that variable gas properties were included.

The conductive-energy terms were evaluated by the method of reference 7 rather than that of reference 6 because of greater accuracy with the former method. When variable gas properties are

included, the equations are as follows:

$$\bar{\Omega}_{e,e} = \int_{\eta_{j,e}}^{\infty} \rho u c_p (T_e - T) dy = \frac{x_e}{\sigma_e} \rho_e u_e R_e T_e \left(1 - \frac{T_b}{T_e}\right) \left(\int_{\eta_{j,e}}^{\eta_{ref}} \frac{\gamma}{\gamma-1} \frac{\varphi}{t_e} d\eta - \int_{\eta_{j,e}}^{\eta_{ref}} \frac{\gamma}{\gamma-1} \frac{\varphi^2}{t_e} d\eta \right)$$

and

$$\bar{\Omega}_{e,i} = \int_{\eta_{i,i}}^{\infty} \rho u c_p (T_i - T) dy = \frac{x_i}{\sigma_i} \rho_i u_i R_i T_i \left(1 - \frac{T_b}{T_i}\right) \left(\int_{\eta_{i,i}}^{\eta_{ref}} \frac{\gamma}{\gamma-1} \frac{\varphi}{t_i} d\eta - \int_{\eta_{i,i}}^{\eta_{ref}} \frac{\gamma}{\gamma-1} \frac{\varphi^2}{t_i} d\eta \right)$$

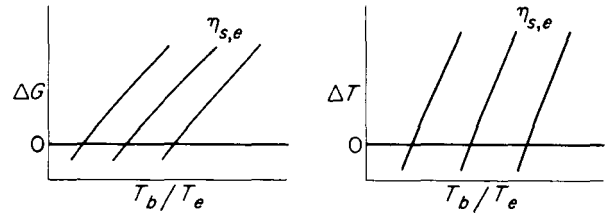
The energy equation could then be written as

$$\Delta E \equiv \frac{\bar{\Omega}_b \sigma_e}{x_e \rho_e u_e R_e T_e} + \left(1 - \frac{T_b}{T_e}\right) \left(\int_{\eta_{i,e}}^{\eta_{ref}} \frac{\gamma}{\gamma-1} \frac{\varphi}{t_e} d\eta - \int_{\eta_{i,e}}^{\eta_{ref}} \frac{\gamma}{\gamma-1} \frac{\varphi^2}{t_e} d\eta + \int_{\eta_{i,e}}^{\eta_{s,e}} \frac{\gamma}{\gamma-1} \frac{\varphi^2}{t_e} d\eta \right) + \frac{T_b}{T_e} \int_{\eta_{i,e}}^{\eta_{s,e}} \frac{\gamma}{\gamma-1} \frac{\varphi}{t_e} d\eta + \frac{x_i}{x_e} \frac{1 - C_e^2}{1 - C_i^2} \frac{C_i}{C_e} \sqrt{\gamma_e - 1} \frac{\gamma_i R_i T_i}{\gamma_e R_e T_e} \left[\left(1 - \frac{T_b}{T_i}\right) \left(\int_{\eta_{i,i}}^{\eta_{ref}} \frac{\gamma}{\gamma-1} \frac{\varphi}{t_i} d\eta - \int_{\eta_{i,i}}^{\eta_{ref}} \frac{\gamma}{\gamma-1} \frac{\varphi^2}{t_i} d\eta + \int_{\eta_{i,i}}^{\eta_{s,i}} \frac{\gamma}{\gamma-1} \frac{\varphi^2}{t_i} d\eta \right) + \frac{T_b}{T_i} \int_{\eta_{i,i}}^{\eta_{s,i}} \frac{\gamma}{\gamma-1} \frac{\varphi}{t_i} d\eta \right]$$

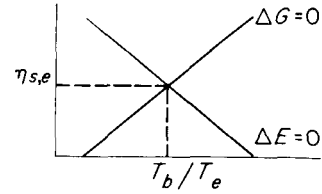
and was evaluated for the assumed values of T_b/T_e and $\eta_{s,e}$.

(h) The solution proceeded by assuming other values of T_b/T_e in step (3)(a), and steps (3)(b) to (g) were repeated until the particular values of T_b/T_e and $\eta_{s,e}$ were determined for which ΔG and ΔE were simultaneously zero. A method that could be used to determine these values was to plot the ΔG and ΔE as a function of T_b/T_e for

constant values of $\eta_{s,e}$ as shown in the following:



A cross plot could then be made of $\eta_{s,e}$ against T_b/T_e for which ΔG and ΔE are zero:



The values of $\eta_{s,e}$ and T_b/T_e at the intersection of the two lines were the solutions for the assumed value of base-pressure ratio. Knowing $\eta_{s,e}$ the limiting-streamline stagnation-pressure ratio (or wake-pressure ratio) was computed by the methods described in step (3)(d).

For the special case where jet-temperature ratio T_i/T_e was 1 and the base energy transfer was zero, the base-gas-temperature ratio T_b/T_e was known, a priori, also to be 1. Therefore it was not necessary to consider the energy-balance equation. The mass-flow balance was still a requirement, but the equation as presented earlier became indeterminate. Hence for calculations where gas properties of the external and internal streams were dissimilar, wake-pressure ratio and base-gas-temperature ratio were determined by extrapolating results for $T_i/T_e > 1$. For calculations where gas properties of both streams were equal, the computing procedure of reference 5 was used.

(4) The stagnation-pressure rise of the limiting streamline from step (3) was compared with the trailing-shock pressure ratio from step (2). If they were not equal, the wrong value of base-pressure ratio had been assumed in step (1), and the solution was repeated for other values of p_b/p_0 until equality was obtained. The base-pressure ratio that was assumed in step (1) to obtain this equality was then the theoretical p_b/p_0 , and the corresponding base gas temperature that was computed in step (3)(h) was the theoretical T_b/T_0 .

APPENDIX C

ANALYTICAL EFFECTS OF INDEPENDENT VARIABLES ON WAKE-PRESSURE RATIO AND BASE-TEMPERATURE RATIO

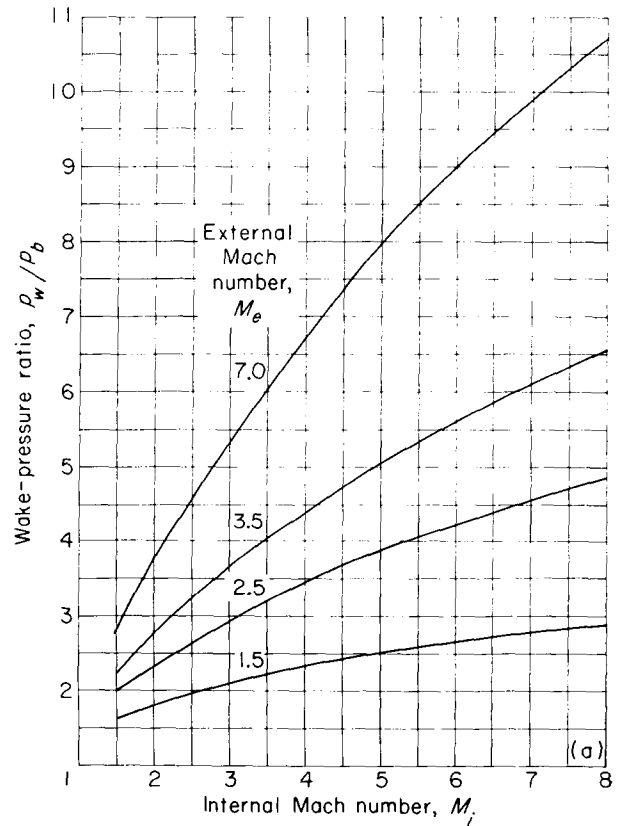
The portion of the analysis described in step (3) of appendix B can be further analyzed by varying the values of the independent parameters, wake-pressure ratio of the limiting streamlines and base-temperature ratio. As discussed in reference 5, base-pressure ratio is related to wake-pressure ratio by the equation $p_b/p_0 = (p_w/p_0)/(p_w/p_b)$. Although p_b/p_0 is a more fundamental base-flow parameter than p_w/p_b , it was desirable for the purposes of this section to analyze p_w/p_b , since it can be considered without regard to model geometry by selecting arbitrary values of M_e and M_i . These results, which are the most difficult part of the base-pressure-ratio determination, may then be used for a specific geometry in the manner described in reference 5.

(5) For this portion of the analysis the following parameters were considered to be independent and specified: M_e , M_i , T_i/T_e , γ_e , R_e , γ_i , R_i , X , m_b , and Ω_b . For these calculations the following approximations were used: $\sigma = 12 + 2.758 M$, $\eta_{ref} = 3$, and $-\infty$ was replaced by -3 . The external stream was assumed to be air.

The effects of varying M_i and M_e for given values of T_i/T_e with an air jet and $X=1$ are shown in figure 25. The results for $T_i/T_e=1$ (fig. 25(a)) were the same as those of reference 5 with the exception that calculations were extended to higher Mach numbers. Results for $T_i/T_e=5$ and 10 are shown in figures 25 (b) to (e). In all cases the trends of the effects were similar and showed: first, an increase in M_i (at constant M_e) increased wake-pressure ratio and decreased base temperature ratio, and, second, an increase in M_e (at constant M_i) increased wake-pressure ratio and base-temperature ratio.

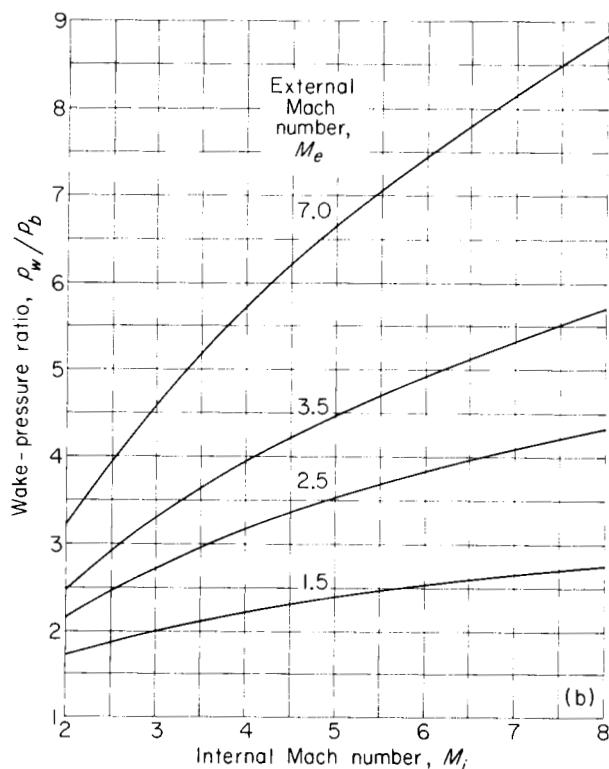
The effects of varying T_i/T_e for various combinations of the values of M_e and M_i are shown in figure 26. For these calculations the values of $\gamma_i=1.24$ and $R_i=2300$ (which are typical for rocket motors using liquid oxygen and RP fuels) were chosen, and again $X=1$. Results for $M_e=$

1.5 (figs. 26 (a) and (b)), $M_e=3$ (figs. 26 (c) and (d)), and $M_e=5$ (figs. 26 (e) and (f)) are shown. The general trend that is apparent in all cases is that an increase in T_i/T_e decreased wake-pressure ratio and increased base-temperature ratio. For values of M_i much larger than that of M_e , the base-temperature-ratio curves for constant values of M_i began to cross over as T_i/T_e increased.



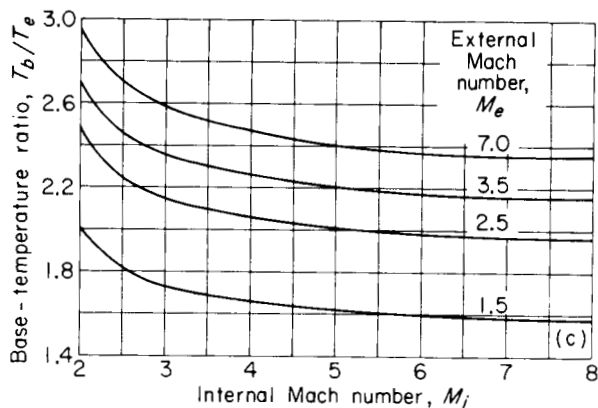
(a) Wake-pressure ratio. Jet-temperature ratio T_i/T_e , 1.

FIGURE 25.—Effect of external and internal Mach numbers on base-flow parameters with air jet. Internal specific-heat ratio γ_i , 1.4; internal gas constant R_i , 1715 ft²/(sec²) (°R); mixing-length ratio X , 1.



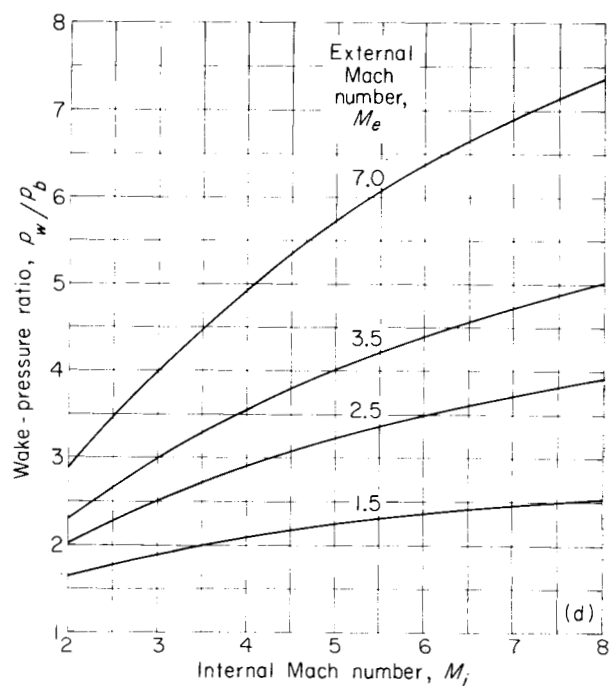
(b) Wake-pressure ratio. Jet-temperature ratio T_i/T_e , 5.

FIGURE 25.—Continued. Effect of external and internal Mach numbers on base-flow parameters with air jet. Internal specific-heat ratio γ_i , 1.4; internal gas constant R_i , 1715 ft²/(sec²) (°R); mixing-length ratio X , 1.



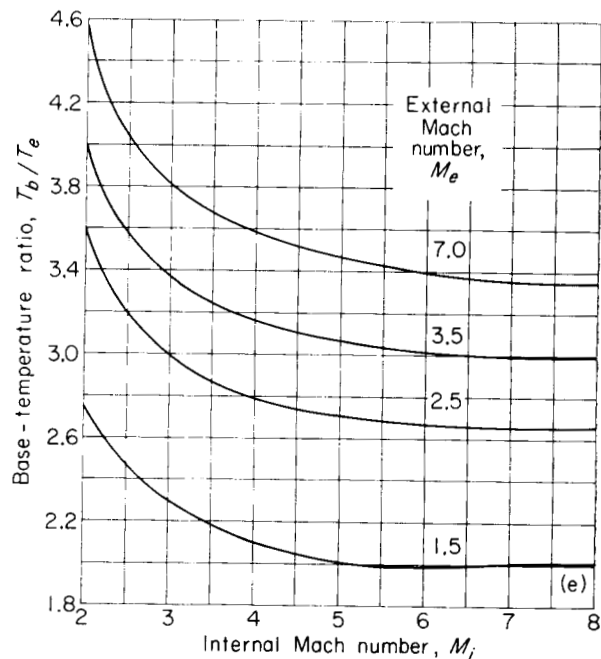
(c) Base-temperature ratio. Jet-temperature ratio T_i/T_e , 5.

FIGURE 25.—Continued. Effect of external and internal Mach numbers on base-flow parameters with air jet. Internal specific-heat ratio γ_i , 1.4; internal gas constant R_i , 1715 ft²/(sec²) (°R); mixing-length ratio X , 1.



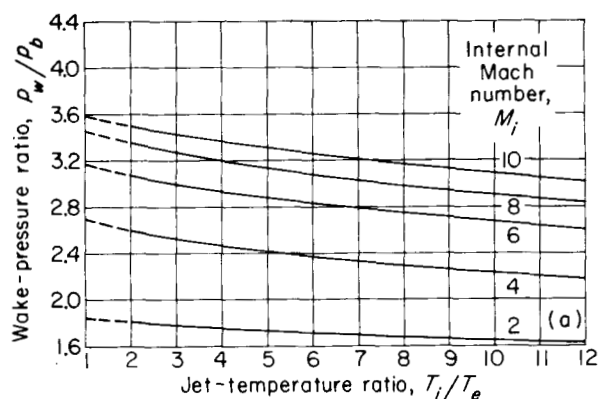
(d) Wake-pressure ratio. Jet-temperature ratio T_i/T_e , 10.

FIGURE 25.—Continued. Effect of external and internal Mach numbers on base-flow parameters with air jet. Internal specific-heat ratio γ_i , 1.4; internal gas constant R_i , 1715 ft²/(sec²) (°R); mixing-length ratio X , 1.



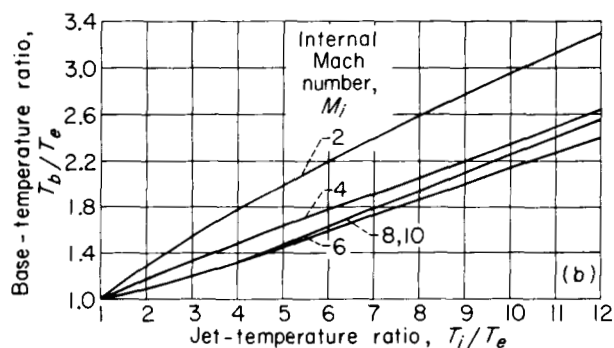
(e) Base-temperature ratio. Jet-temperature ratio T_i/T_e , 10.

FIGURE 25.—Concluded. Effect of external and internal Mach numbers on base-flow parameters with air jet. Internal specific-heat ratio γ_i , 1.4; internal gas constant R_i , 1715 ft²/(sec²) (°R); mixing-length ratio X , 1.



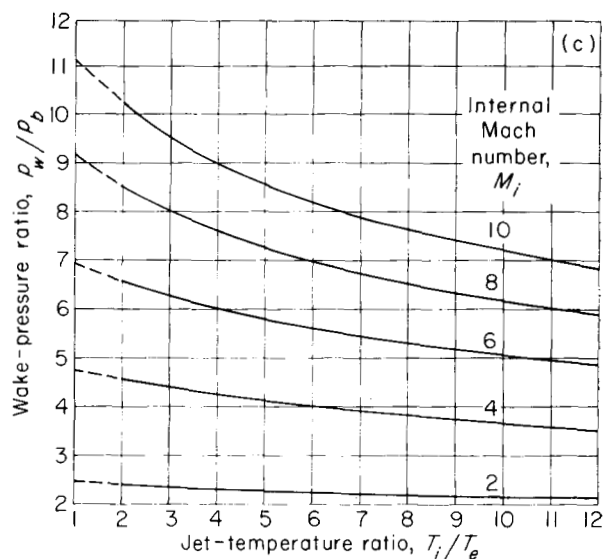
(a) Wake-pressure ratio. External Mach number M_e , 1.5.

FIGURE 26.—Effect of jet-temperature ratio on base-flow parameters. Internal specific-heat ratio γ_i , 1.24; internal gas constant R_i , 2300 ft²/(sec²)(°R); mixing-length ratio X , 1.



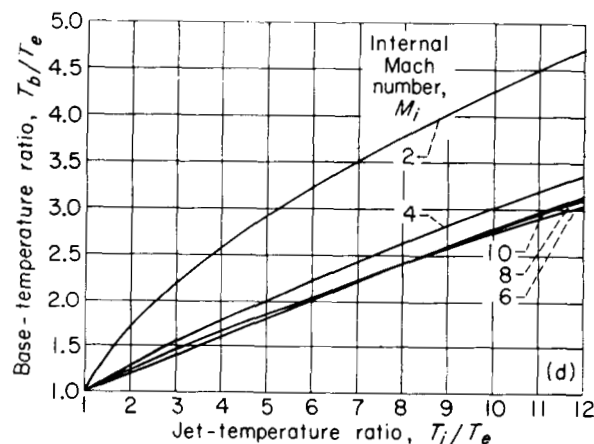
(b) Base-temperature ratio. External Mach number M_e , 1.5.

FIGURE 26.—Continued. Effect of jet-temperature ratio on base-flow parameters. Internal specific-heat ratio γ_i , 1.24; internal gas constant R_i , 2300 ft²/(sec²)(°R); mixing-length ratio X , 1.



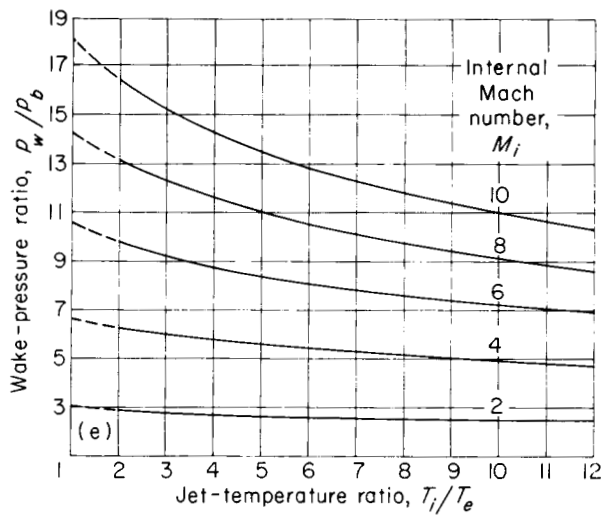
(c) Wake-pressure ratio. External Mach number M_e , 3.

FIGURE 26.—Continued. Effect of jet-temperature ratio on base-flow parameters. Internal specific-heat ratio γ_i , 1.24; internal gas constant R_i , 2300 ft²/(sec²)(°R); mixing-length ratio X , 1.



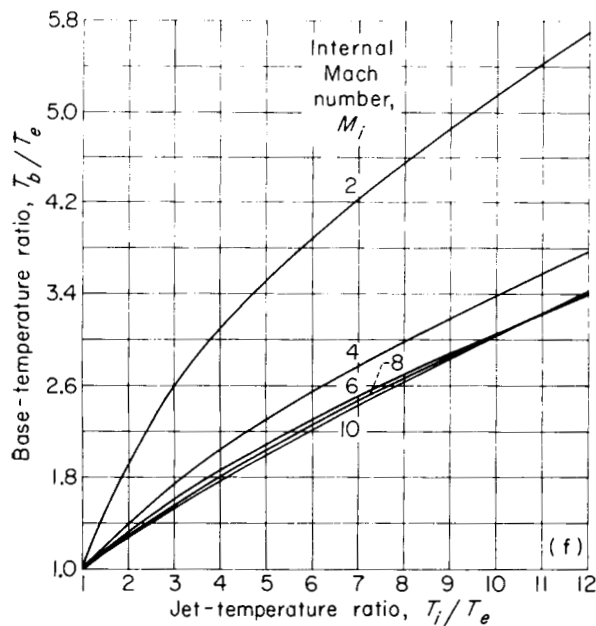
(d) Base-temperature ratio. External Mach number M_e , 3.

FIGURE 26.—Continued. Effect of jet-temperature ratio on base-flow parameters. Internal specific-heat ratio γ_i , 1.24; internal gas constant R_i , 2300 ft²/(sec²)(°R); mixing-length ratio X , 1.



(e) Wake-pressure ratio. External Mach number M_e , 5.

FIGURE 26.—Continued. Effect of jet-temperature ratio on base-flow parameters. Internal specific-heat ratio γ_i , 1.24; internal gas constant R_i , 2300 ft²/(sec²)(°R); mixing-length ratio X , 1.



(f) Base-temperature ratio. External Mach number M_e , 5.

FIGURE 26.—Concluded. Effect of jet-temperature ratio on base-flow parameters. Internal specific-heat ratio γ_i , 1.24; internal gas constant R_i , 2300 ft²/(sec²)(°R); mixing-length ratio X , 1.

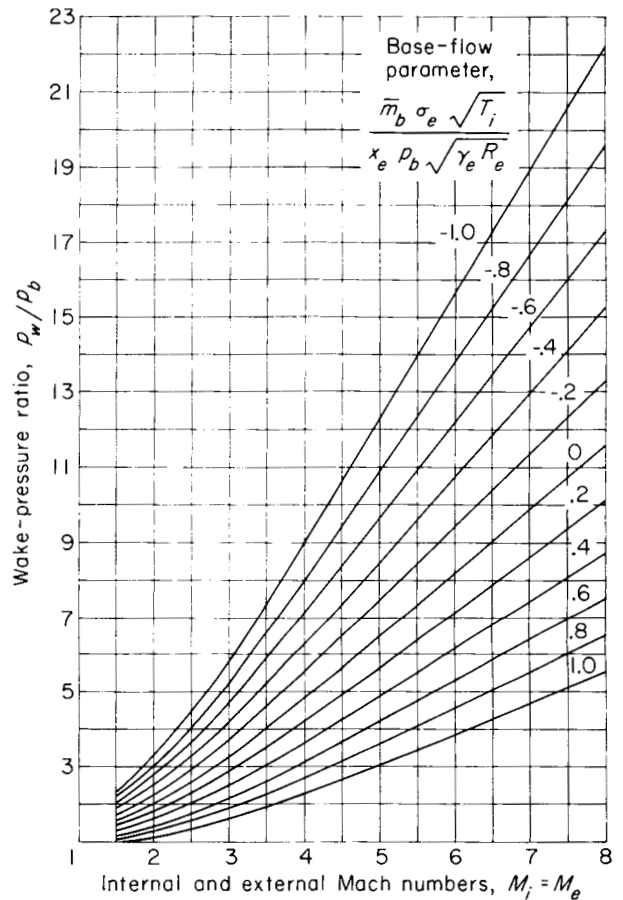


FIGURE 27.—Effect of base bleed on wake-pressure ratio. Jet-temperature ratio T_i/T_e , 1; internal and external specific-heat ratios γ_i and γ_e , 1.4; internal and external gas constants R_i and R_e , 1715 ft²/(sec²)(°R); mixing-length ratio X , 1.

It is doubtful that this crossover should occur, and it may have been a result of inadequacies of the computing procedure. However, the degree of crossover was not large, and the trends of the results were still valid.

Base-bleed effects on the wake-pressure ratio associated with an air jet are shown in figure 27. For this calculation T_i/T_e was chosen to be 1, and the base-bleed gas was air at the same total temperature as the internal and external streams. To reduce the number of computations required, the restriction was imposed that $M_e = M_i$. As in earlier figures, $X=1$. The results show that, at any given value of Mach number, positive base

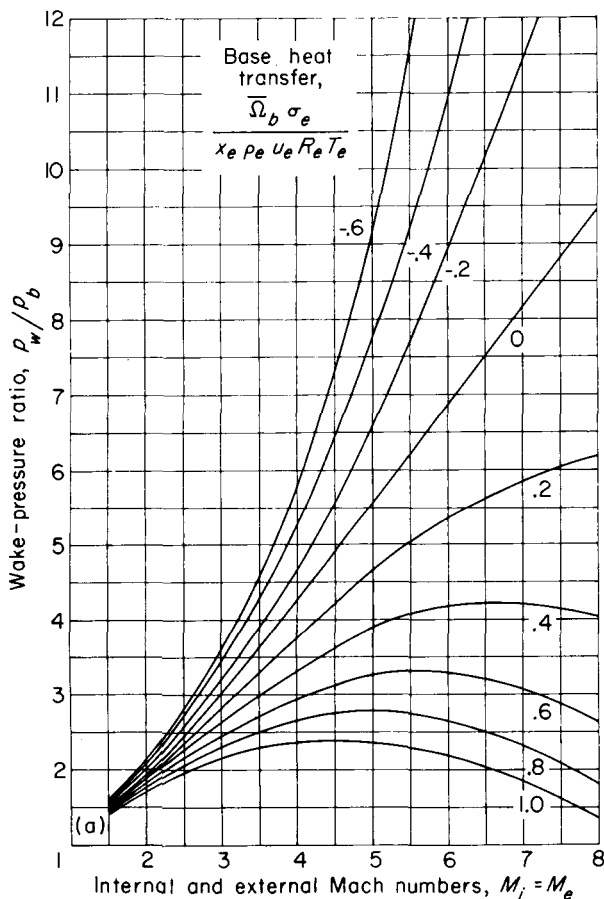
bleed decreased wake-pressure ratio, and negative base bleed (removing air from the base region) increased wake-pressure ratio.

Effects of energy transfer (heat addition or subtraction) in the base region are shown in figure 28 for an air jet with $T_i/T_e=5$. As in the previous figure, $M_e=M_i$ and $X=1$. Heat removal increased wake-pressure ratio and decreased base temperature, and energy addition decreased wake-pressure ratio and increased base-temperature ratio.

To determine the magnitude of the dependent parameters p_w/p_b and T_b/T_0 for a typical missile flight, an estimate was made of the range of the variables M_e , M_i , and T_i/T_0 for typical missile

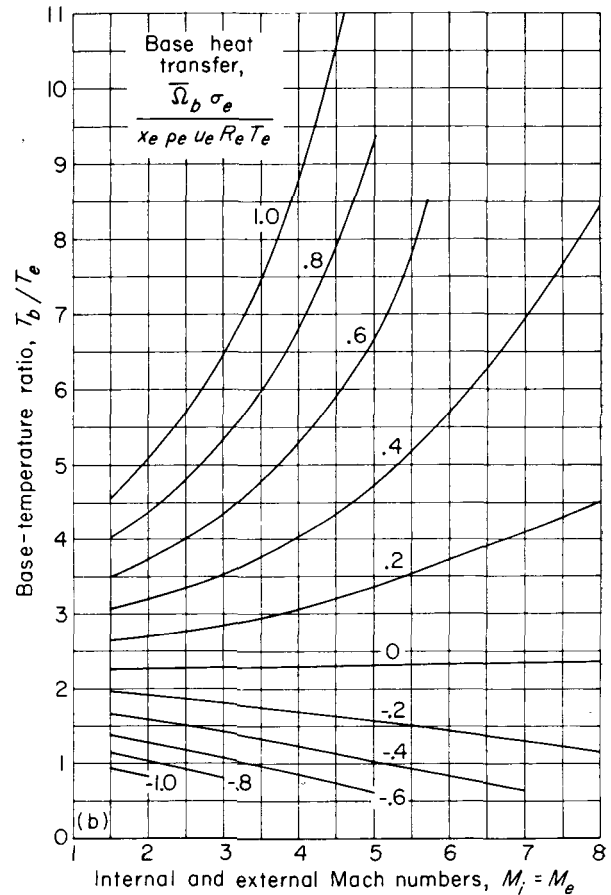
trajectories. These estimates are shown in figure 29. In the figures that follow, figure 29 was used as a guide in selecting values of the variables in the range of interest.

Anticipated values of wake-pressure ratio and base-temperature ratio for typical trajectories are shown in figure 30. For these calculations values of internal gas properties (γ and R) were selected which were representative of those for propellant motors using liquid oxygen and RP fuels, and X was assumed to be 1. For selected values of M_e , the variables M_i and T_i/T_0 were varied over the range of interest. These results show that wake-pressure ratio increases rapidly with external Mach number and is more insensitive to changes



(a) Wake-pressure ratio.

FIGURE 28.—Effect of base heat transfer. Jet-temperature ratio T_i/T_e , 5; internal and external specific-heat ratios γ_i and γ_e , 1.4; internal and external gas constants R_i and R_e , 1715 ft²/(sec²)(°R); mixing-length ratio X , 1; bleed-mass-flow rate m_b , 0.



(b) Base-temperature ratio.

FIGURE 28.—Concluded. Effect of base heat transfer. Jet-temperature ratio T_i/T_e , 5; internal and external specific-heat ratios γ_i and γ_e , 1.4; internal and external gas constants R_i and R_e , 1715 ft²/(sec²)(°R); mixing-length ratio X , 1; bleed-mass-flow rate m_b , 0.

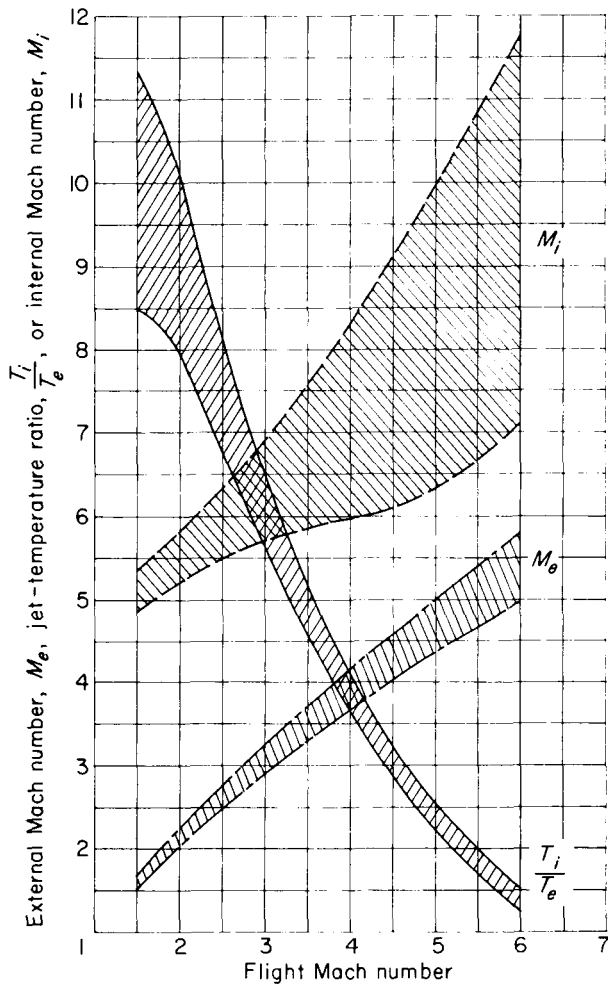
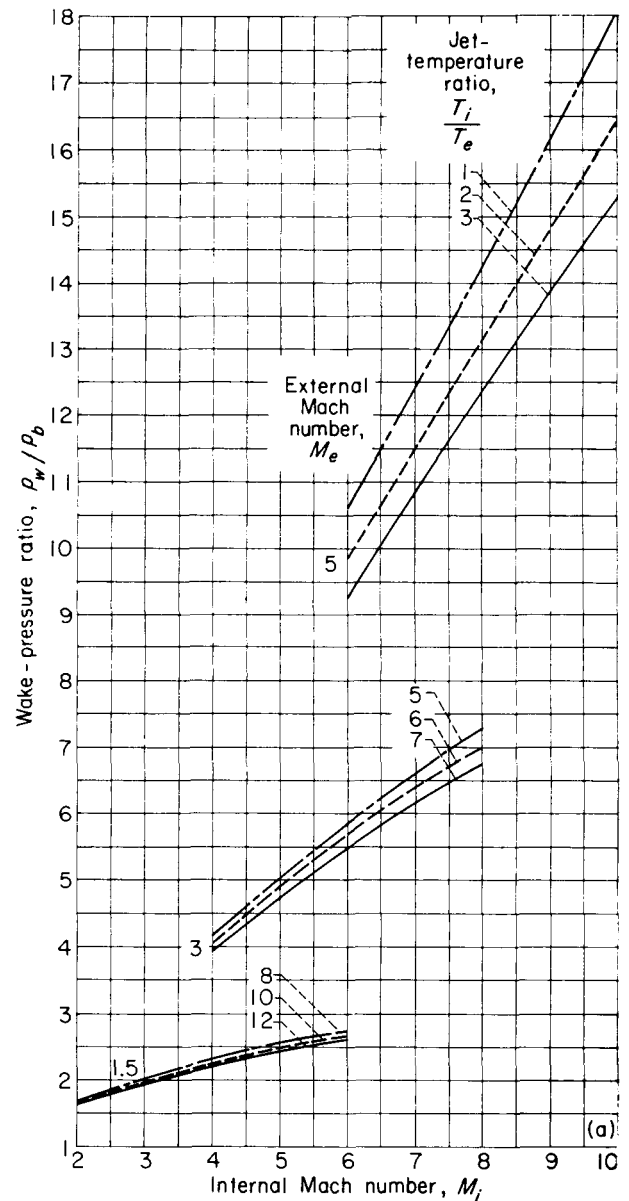


FIGURE 29.—Estimated range of variables for typical missile trajectories.

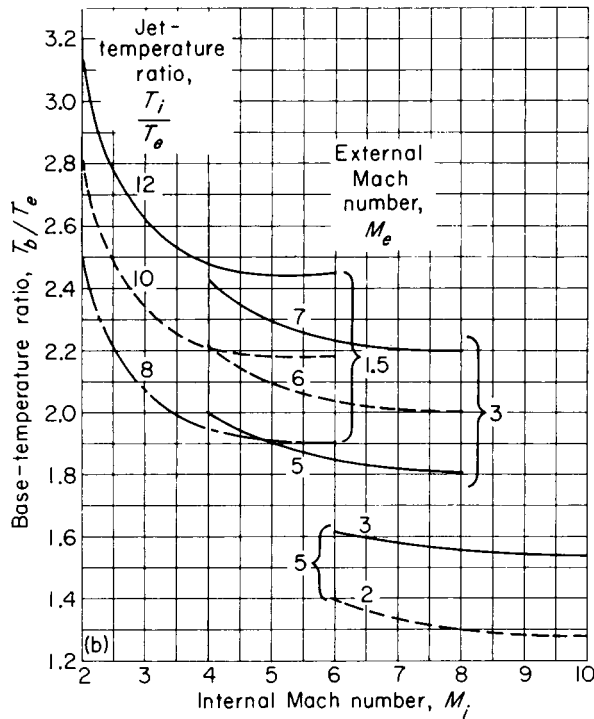
in M_i and T_i/T_0 at low values of M_e than at high values (fig. 30(a)). Base-temperature ratio decreased as M_e increased and was much less sensitive to changes in M_i than to changes in T_i/T_0 (fig. 30(b)).

Effects on base-flow parameters of varying internal specific-heat ratio γ_i , internal gas constant R_i , and mixing-length ratio X are shown in figures 31 to 33. Specific combinations of the



(a) Wake-pressure ratio.

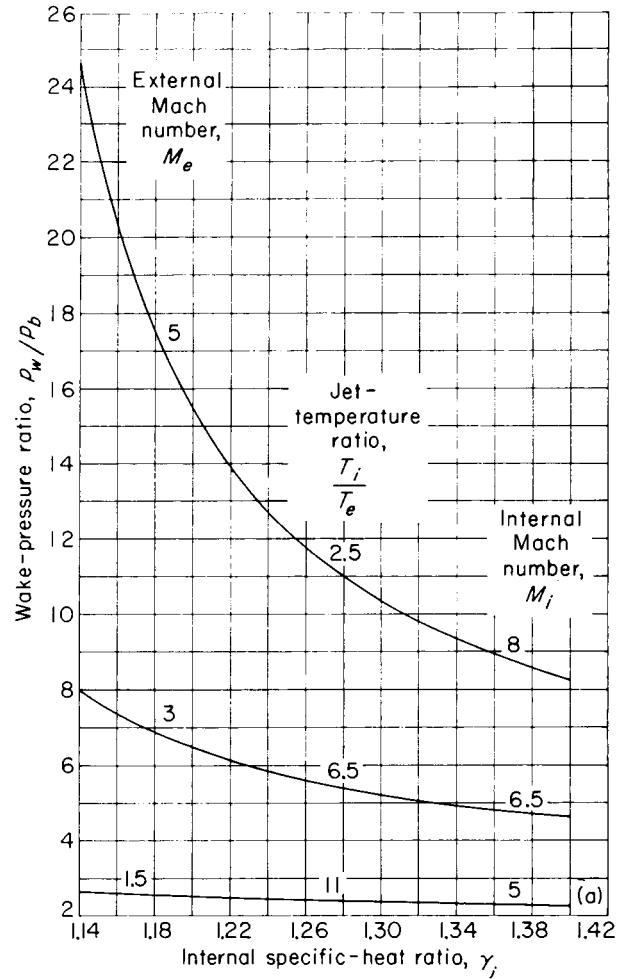
FIGURE 30.—Range of base-flow parameters for typical trajectories. Internal specific-heat ratio γ_i , 1.24; internal gas constant R_i , 2300 ft²/(sec²)(°R); mixing-length ratio X , 1.



(b) Base-temperature ratio.

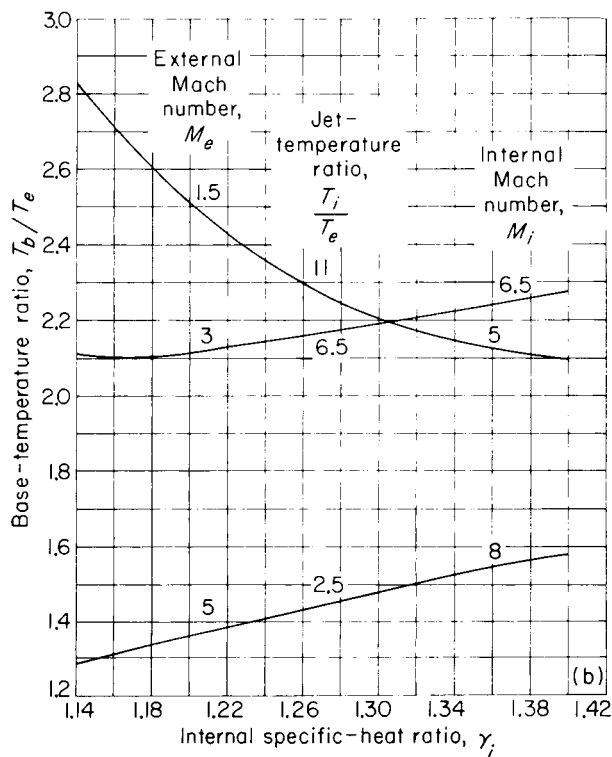
FIGURE 30.—Concluded. Range of base-flow parameters for typical trajectories. Internal specific-heat ratio γ_i , 1.24; internal gas constant R_i , 2300 ft²/(sec²)(°R); mixing-length ratio X , 1.

values of M_e , M_i , and T_i/T_0 which were within the range of interest were selected for these figures. Effects of γ_i are shown in figure 31 for $R_i=2300$ and $X=1$. For all combinations of the parameters, wake-pressure ratio decreased as γ_i increased and varied at a much faster rate for



(a) Wake-pressure ratio.

FIGURE 31.—Effect of internal specific-heat ratio on base-flow parameters. Internal gas constant R_i , 2300 ft²/(sec²)(°R); mixing-length ratio X , 1.

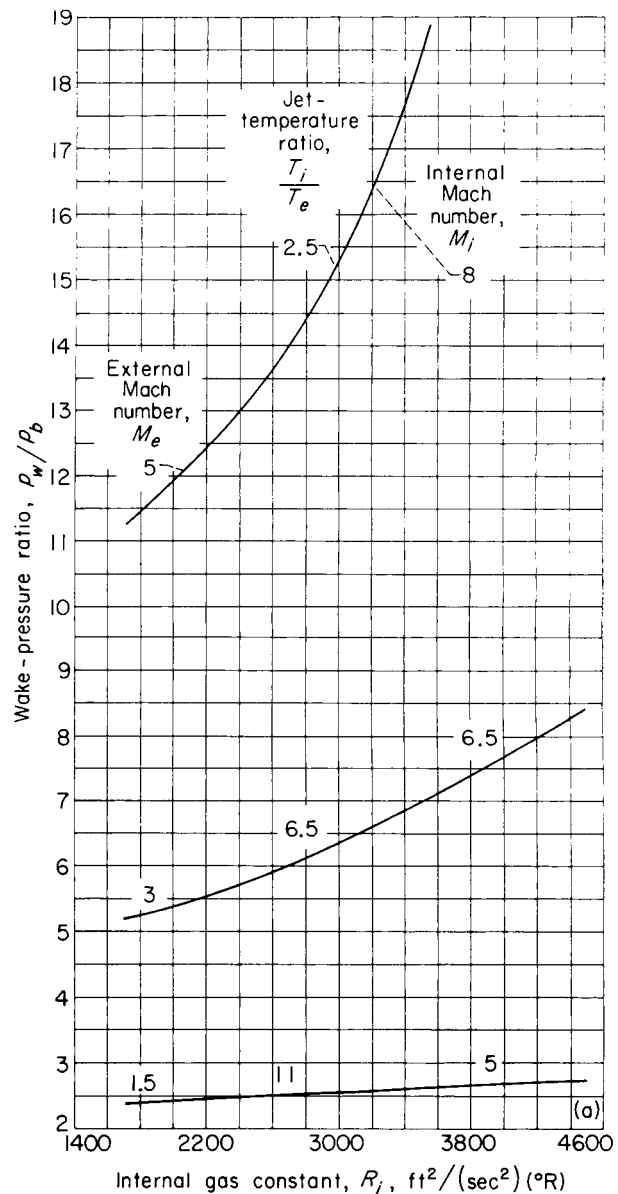


(b) Base-temperature ratio.

FIGURE 31.—Concluded. Effect of internal specific-heat ratio on base-flow parameters. Internal gas constant R_i , 2300 ft²/(sec²)(°R); mixing-length ratio X , 1.

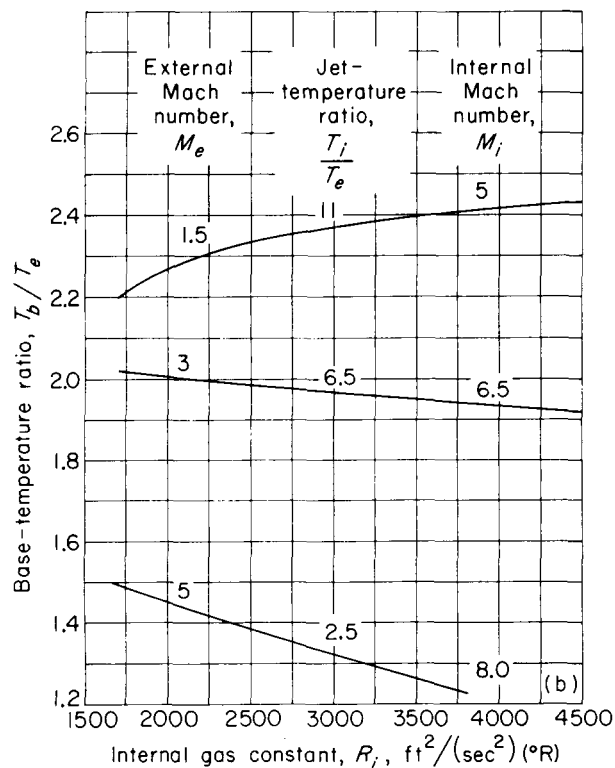
the conditions specified at higher values of M_e than at the lower values (fig. 31(a)). However, the direction of the variation of base-temperature ratio depended upon the magnitude of the other parameter (fig. 31(b)); at $M_e=1.5$ it decreased as γ_i increased, and at $M_e=3$ and 5 it increased.

In a similar manner, effects of varying R_i are shown in figure 32. For these results X was again 1 and $\gamma_i=1.24$ was chosen. Conversely to the effect of γ_i , increases in R_i increased wake-pressure ratio (fig. 32(a)) for each combination of the parameters. Again the rate of change with



(a) Wake-pressure ratio.

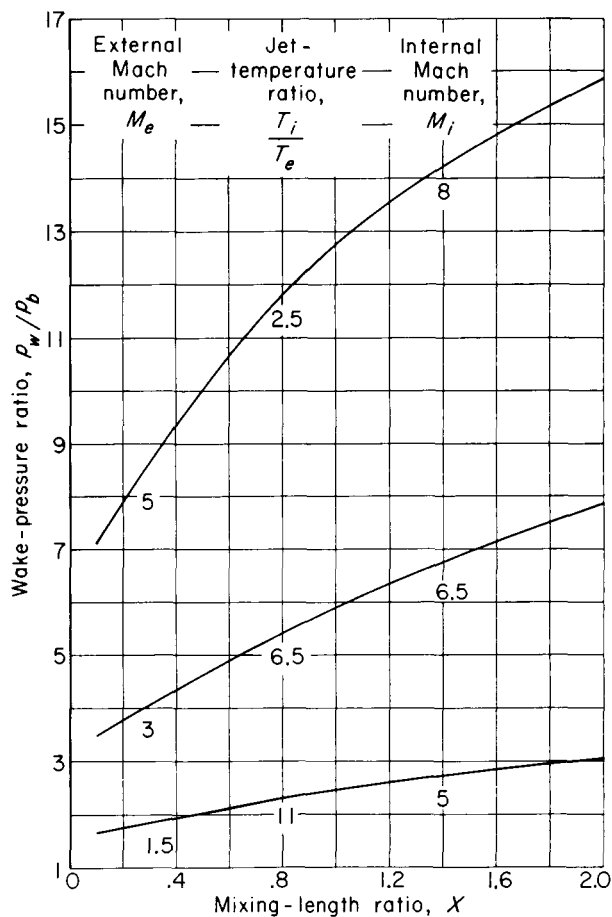
FIGURE 32.—Effect of internal gas constant on base-flow parameters. Internal specific-heat ratio γ_i , 1.24; mixing-length ratio X , 1.



(b) Base-temperature ratio.

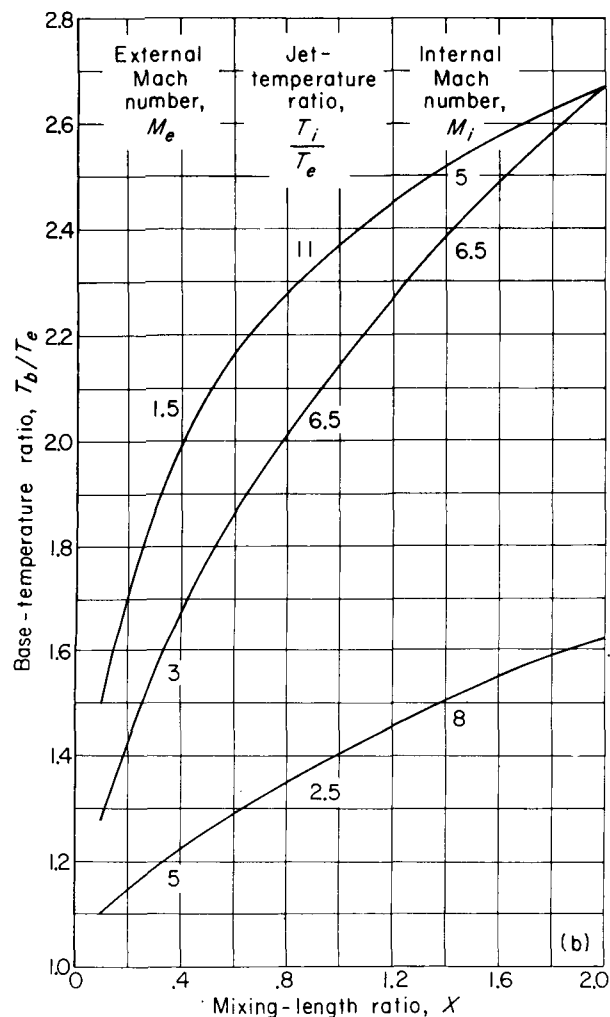
 FIGURE 32.—Concluded. Effect of internal gas constant on base-flow parameters. Internal specific-heat ratio γ_i , 1.24; mixing-length ratio X , 1.

R_i was greater for the conditions specified at the higher values of M_e than at the lower values. Similarly the direction of the variation of base-temperature ratio with changes in R_i depended



(a) Wake-pressure ratio.

 FIGURE 33.—Effect of mixing-length ratio on base-flow parameters. Internal specific-heat ratio γ_i , 1.24; internal gas constant R_i , 2300 $\text{ft}^2/(\text{sec}^2)(^\circ\text{R})$.



(b) Base-temperature ratio.

FIGURE 33.—Concluded. Effect of mixing-length ratio on base-flow parameters. Internal specific-heat ratio γ_i , 1.24; internal gas constant R_i , 2300 ft²/(sec²) (°R).

upon the magnitude of the other parameters (fig. 32(b)) but varied in the opposite direction to that shown for γ_i effects. At $M_e=1.5$ base-temperature ratio increased with increases in R_i , and at $M_e=3$ and 5 it decreased.

Effects of varying the mixing-length ratio are shown in figure 33 for $\gamma_i=1.24$ and $R_i=2300$. In all cases both wake-pressure ratio and base-temperature ratio increased with increases in X . Beneficial cooling effects of extending the motor downstream of the base are obvious in the figure.

REFERENCES

1. Chapman, Dean R.: Laminar Mixing of a Compressible Fluid. NACA Rep. 958, 1950. (Supersedes NACA TN 1800.)
2. Korst, H. H., Page, R. H., and Childs, M. E.: A Theory for Base Pressures in Transonic and Supersonic Flow. Tech. Note 392-2, Eng. Exp. Station, Univ. Ill., Mar. 1955.
3. Chow, W. L.: On the Base Pressure Resulting from the Interaction of a Supersonic External Stream with a Sonic or Subsonic Jet. Jour. Aero/Space Sci., vol. 26, no. 3, Mar. 1959, pp. 176-180.
4. Beheim, Milton A.: Flow in the Base Region of Axisymmetric and Two-Dimensional Configurations. NASA TR R-77, 1961.
5. Baughman, L. Eugene, and Kochendorfer, Fred D.: Jet Effects on Base Pressures of Conical Afterbodies at Mach 1.91 and 3.12. NACA RM E57E06, 1957.
6. Page, Robert Henry: The Non-Isoenergetic Turbulent Jet Mixing of a Two Dimensional Supersonic Jet with Consideration of Its Influence on the Base Pressure Problem. Ph.D. Thesis, Univ. Ill., 1955.
7. Korst, H. H., and Chow, W. L.: Compressible Non-Isoenergetic Two-Dimensional Turbulent ($Pr_t=1$) Jet Mixing at Constant Pressure—Auxiliary Integrals, Heat Transfer, and Friction Coefficients for Fully Developed Mixing Profiles. Tech. Note 392-4, Eng. Exp. Station, Univ. Ill., Jan. 1959.
8. Foelsch, Kuno: The Analytical Design of an Axially Symmetric Laval Nozzle for a Parallel and Uniform Jet. Jour. Aero. Sci., vol. 16, no. 3, Mar. 1949, pp. 161-166.
9. Runckel, Jack F., and Swihart, John M.: A Hydrogen Peroxide Turbojet-Engine Simulator for Wind-Tunnel Powered-Model Investigations. NACA RM L57H115, 1957.
10. Clippinger, R. F.: Supersonic Axially Symmetric Nozzles. Rep. 794, Ballistic Res. Lab., Aberdeen Proving Ground (Md.), Dec. 1951.
11. Sims, Joseph L.: Results of the Computations of Supersonic Flow Fields Aft of Circular Cylindrical Bodies of Revolution by the Method of Characteristics. Rep. DA-R-49, Army Ballistic Missile Agency, Mar. 17, 1958.
12. Love, Eugene S., Grigsby, Carl E., Lee, Louise P., and Woodling, Mildred J.: Experimental and Theoretical Studies of Axisymmetric Free Jets. NASA TR R-6, 1959. (Supersedes NACA RM's L54L31, L55J14, L56G18, and TN 4195.)
13. Englert, Gerald W.: Operational Method of Determining Initial Contour of and Pressure Field about a Supersonic Jet. NASA TN D-279, 1960.
14. Wimbrow, William R.: Effects of Base Bleed on the Base Pressure of Blunt-Trailing-Edge Airfoils at Supersonic Speeds. NACA RM A54A07, 1954.
15. Wu, Chen Yuan: The Influence of Finite Bleed Velocities on the Effectiveness of Base Bleed in the Two Dimensional Supersonic Base Pressure Problem. Ph. D. Thesis, Univ. Ill., 1957.